Acta Pharmaceutica Sinica B 2026;16(1):555−573

Chinese Pharmaceutical Association
Institute of Materia Medica, Chinese Academy of Medical Sciences

Acta Pharmaceutica Sinica B

www.elsevier.com/locate/apsb
www.sciencedirect.com

ORIGINAL ARTICLE

Photoimmunological hydrogel vaccine creates a supportive immune niche to promote antigen cross-presentation cascade and cancer-immunity cycle progression

Hanxi Zhang[a,†], Jiazhen Lv[a,†], Wanyi Zhou[a], Jiangping Lei[a], Yu Yang[a], Jianqiao Kong[b], Chunhui Wu[a], Chuan Zheng[b,*], Fengming You[b,*], Yiyao Liu[a,b,c,d,*], Hong Yang[a,*]

[a]*Department of Medical Oncology, Sichuan Clinical Research Center for Cancer, Sichuan Cancer Hospital & Institute, Sichuan Cancer Center, and School of Life Science and Technology, University of Electronic Science and Technology of China, Chengdu 610054, China*
[b]*Traditional Chinese Medicine (TCM) Prevention and Treatment of Metabolic and Chronic Diseases Key Laboratory of Sichuan Province, Hospital of Chengdu University of Traditional Chinese Medicine, Chengdu 610072, Sichuan, China*
[c]*Department of Otorhinolaryngology, Hospital of Chengdu University of Traditional Chinese Medicine, Chengdu 610072, China*
[d]*Department of Urology, Deyang People's Hospital, Deyang 618099, China*

Received 8 February 2025; received in revised form 30 April 2025; accepted 16 June 2025

KEY WORDS

Cancer immunotherapy;
Therapeutic tumor vaccines;
Immunogenic cell death;
Dendritic cell recruitment;
Ovalbumin;
Resiquimod;

Abstract Therapeutic tumor vaccines have emerged as promising weapons for inducing robust and durable antitumor immune responses, demonstrating substantial potential for cancer treatment. However, clinical efficacy is significantly hindered by tumor immunogenicity scarcity, antigen presentation deficiency, and immunosuppressive tumor microenvironment. To surmount these obstacles, we proposed an injectable photoimmunological hydrogel vaccine (CRPO/G@ALG) to improve immunotherapy outcomes through the dual mechanism of immunogenic cell death (ICD) induction and dendritic cell (DC) recruitment. The model antigen ovalbumin (OVA) and toll-like receptor 7/8 agonist resiquimod (R848) were incorporated into photothermal copper sulfide nanoparticles (CuS) to construct the

*Corresponding authors.
E-mail addresses: zhengchuan@cdutcm.edu.cn (Chuan Zheng), yfmdoc@163.com (Fengming You), liuyiyao@uestc.edu.cn (Yiyao Liu), yanghongyh@uestc.edu.cn (Hong Yang).
[†]These authors made equal contributions to this work.
Peer review under the responsibility of Chinese Pharmaceutical Association and Institute of Materia Medica, Chinese Academy of Medical Sciences.

https://doi.org/10.1016/j.apsb.2025.10.024

Granulocyte-macrophage colony-stimulating factor;
Sodium alginate

nanovaccine CRPO, which was subsequently encapsulated with the granulocyte-macrophage colony-stimulating factor (GM-CSF) in sodium alginate (ALG) to form the hydrogel vaccine CRPO/G@ALG. Following peritumoral administration, CRPO/G@ALG undergoes gelation in response to physiological calcium ions, facilitating the localized retention and controlled release of payloads. Near-infrared (NIR) irradiation triggers ICD in tumor cells, generating an *in situ* antigen reservoir enriched with tumor-associated antigens (TAAs) to bolster tumor immunogenicity. Concurrently, GM-CSF attracts DCs to infiltrate tumor tissues, while R848 promotes DC maturation and antigen cross-presentation. These synergistic effects prolong the duration of immune stimulation and expand both the breadth and depth of antitumor immunity. In 4T1 tumor-bearing mice, CRPO/G@ALG effectively suppressed primary and distant tumor growth and markedly reduced lung metastasis. Collectively, our findings illustrate the transformative potential of integrating ICD induction, DC recruitment, and hydrogel delivery systems, offering new avenues to advance therapeutic tumor vaccine applications.

1. Introduction

Cancer immunotherapy revolutionized malignancy treatment by harnessing the immune system to recognize and eliminate cancer cells. Central to its success is the concept of the cancer−immunity cycle, which encompasses the sequential stages of antigen release, presentation, immune activation, and tumor destruction[1,2]. Upon cancer cell death, autologous neoantigens are released, priming the new round of the cancer−immunity cycle to establish a supportive immune niche[3]. Advances in understanding this underlying mechanism have facilitated the development of diverse immunotherapeutic approaches, including cytokines, immune checkpoint inhibitors, adoptive cell transfer, and tumor vaccines[4-7]. These therapies target distinct stages of the cancer−immunity cycle and have demonstrated significant clinical potential. Nevertheless, triple-negative breast cancer (TNBC), notable for its heterogeneity and aggressiveness, remains the most challenging and resistant subtype of breast cancer in clinical practice[8-11]. The limited response of TNBC to immunotherapy is primarily attributed to poor tumor immunogenicity, inadequate antigen presentation, and the immunosuppressive tumor microenvironment (TME)[12,13]. These limitations highlight the urgent need for innovative therapeutic strategies to overcome immune paralysis and improve the suboptimal prognosis of TNBC treatments.

Combining immunotherapy with complementary treatment modalities has emerged as a promising strategy to enhance therapeutic efficacy against refractory cancers. Photothermal therapy (PTT)-induced immunogenic cell death (ICD) not only eradicates cancer cells directly but also induces the release of damage-associated molecular patterns (DAMPs) and tumor-associated antigens (TAAs)[14,15]. This approach generates vaccine-like immune responses, contributes to converting the immunologically inert "cold" TME into an active "hot" state, and creates an *in situ* antigen depot to supply autologous antigens, thereby reshaping unfavorable TME and enhancing tumor immunogenicity[16,17]. However, defective antigen presentation becomes another critical bottleneck for adaptive antitumor immunity initiation[18-20]. Dendritic cells (DCs), as pivotal mediators of antigen capture, processing, and presentation, are often rendered dysfunctional by tumor-driven immunosuppression[21-24]. To address these barriers, adjuvants such as granulocyte-macrophage colony-stimulating factor (GM-CSF) and the toll-like receptor 7/8 (TLR7/TLR8) agonist resiquimod (R848) have been explored for promoting DC recruitment, maturation, and migration[25-30]. Given that anticancer immunity activation involves a cascade of intricate processes, simultaneously targeting multiple stages of the cancer-immunity cycle is essential for achieving improved therapeutic outcomes. In this context, the invention of multifunctional engineering formulations capable of orchestrating comprehensive and synchronized immune stimulation represents a promising yet challenging frontier. Nanocomposite-based therapeutic tumor hydrogel vaccines have provided demonstrative solutions[31-34]. Specifically, nanovaccines incorporate antigens and adjuvants to train and activate immune cells, eliciting potent and durable tumor rejection[35,36]. Meanwhile, hydrogel systems function as reservoirs for nanovaccines, enabling localized and sustained payload release following *in situ* administration or implantation at lesion sites[37-39]. These composite platforms considerably optimize payload delivery and avoid the inconvenience of frequent vaccinations.

In order to overcome the intrinsic obstacle in TNBC immunotherapy, this study developed an injectable photoimmunological hydrogel vaccine (CRPO/G@ALG) to enhance therapeutic efficacy through the dual mechanism of immunogenic cell death induction and dendritic cell recruitment (Scheme 1). The model antigen ovalbumin (OVA) and agonist adjuvant R848 were incorporated into the photothermal copper sulfide nanoparticles (CuS) to fabricate a novel nanovaccine CRPO. Subsequently, GM-CSF and CRPO were embedded into sodium alginate hydrogel (ALG) to form the hydrogel vaccine CRPO/G@ALG. After peritumoral administration, CRPO/G@ALG achieves physiological calcium ion-responsive gelation, enabling localized anchoring and sustained release of payloads. The released GM-CSF recruits DCs into TMEs, enhancing the tumor infiltration of antigen-presenting cells (APCs). Simultaneously, the liberated CRPO gradually internalized into tumor cells to trigger ICD upon near-infrared irradiation (NIR), establishing an *in situ* antigen reservoir that affords exogenous and autologous antigens. This regimen creates a supportive immune niche at tumor sites, expands the antigen repertoire, and upgrades antigen presentation, resulting in a more robust and comprehensive antitumor immune response to defeat cancer. Overall, CRPO/G@ALG combines the advantages of hydrogel and nanovaccines, targeting multiple stages of the cancer immunity cycle, priming reinforced and lasting antitumor immunity. This research offers a novel perspective and an exploratory paradigm for advancing hydrogel vaccine innovation.

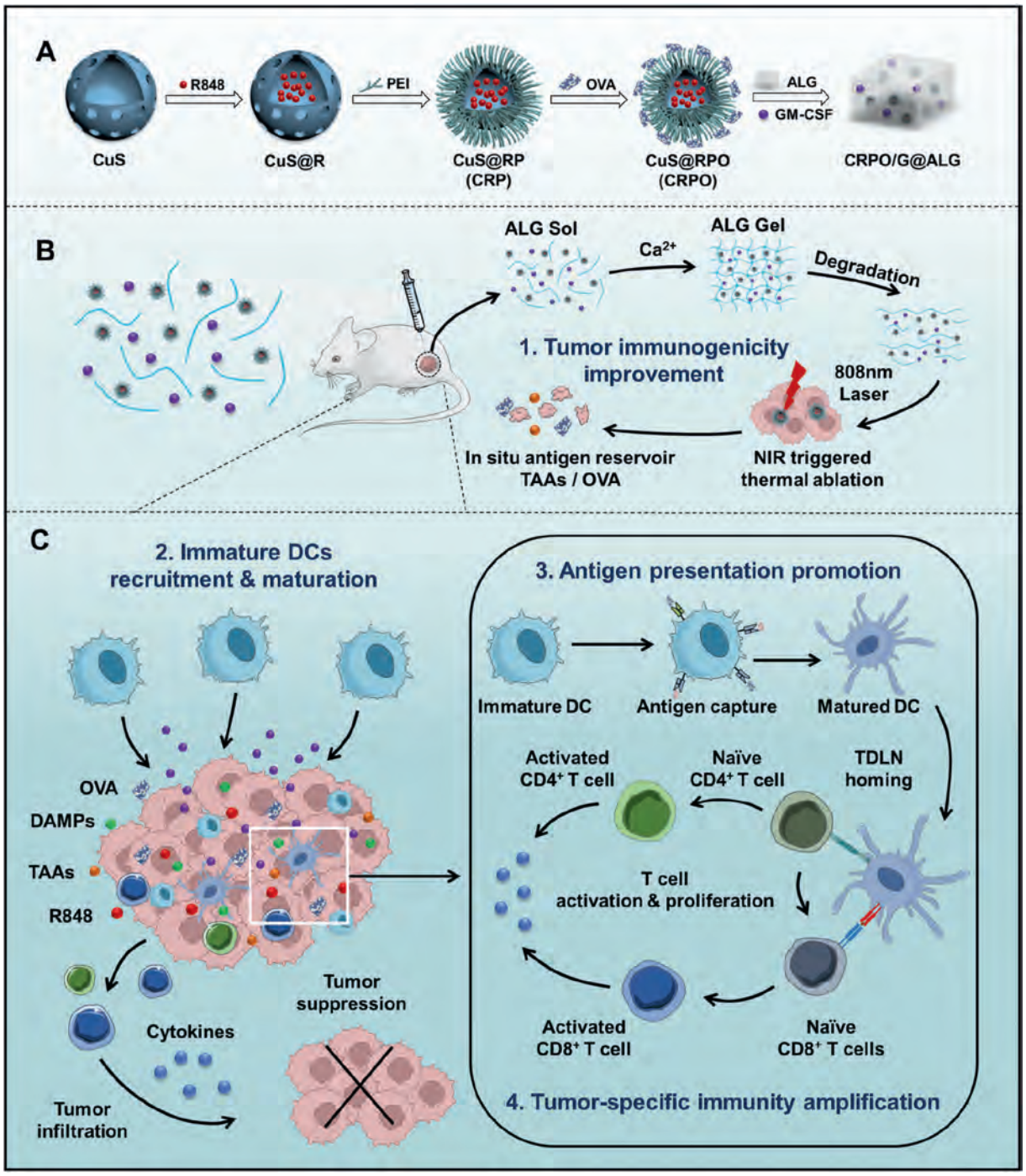

Scheme 1 Schematic illustration of the preparation and antitumor mechanism of the therapeutic hydrogel vaccine CRPO/G@ALG. (A) The detailed fabrication procedure of CRPO/G@ALG. (B) *In situ* gelation, degradation, and vaccination of CRPO/G@ALG. (C) The underlying mechanism of CRPO/G@ALG-mediated efficient photoimmunotherapy by immunogenic cell death induction and dendritic cell recruitment.

2. Materials and methods

2.1. Chemicals and reagents

Polyvinylpyrrolidone (PVP-K30), copper(II) chloride dihydrate ($CuCl_2 \cdot 2H_2O$), hydrazine hydrate ($N_2H_4 \cdot H_2O$), sodium sulfide (Na_2S), sodium alginate (ALG), and anhydrous calcium chloride ($CaCl_2$) were purchased from Aladdin (Shanghai, China). Polyethyleneimine (PEI), ovalbumin (OVA), and indocyanine green (ICG) were obtained from Sigma−Aldrich (Saint Louis, MO, USA). Resiquimod (R848) was acquired from Solarbio (Beijing, China). The Cell Counting Kit-8 (CCK-8) assay kit, Calcein/propidium iodide (PI) staining assay kit, Annexin V-FITC/PI staining kit, Bicinchoninic acid (BCA) protein assay kit, nuclear dyes 4′,6-diamidino-2mlphenylindole (DAPI) and Hoechst 33342 (Hoechst), and Lyso-Tracker Red were procured from Beyotime (Shanghai, China). Granulocyte-macrophage colony-stimulating factor (GM-CSF) was purchased from NeoBioscience (Shenzhen,

China). The enzyme-linked immunosorbent assay (ELISA) kit was obtained from Abclonal (Wuhan, China). Antibodies used for immunofluorescence, immunohistochemistry, and flow cytometry analysis sourced from Thermo Fisher Scientific (Waltham, MA, USA). All chemicals and reagents were used as received, following the manufacturer's instructions.

2.2. Cells and animals

Murine breast cancer cell lines 4T1 and EMT-6, mouse fibroblast NIH3T3 cells, and dendritic cell line DC 2.4 were obtained from the Chinese Academy of Sciences (Shanghai, China) and EK-Bioscience (Shanghai, China), respectively. 4T1, EMT-6, and DC 2.4 cells were cultured in Roswell Park Memorial Institute (RPMI) 1640 medium, while NIH3T3 cells were cultured in Dulbecco's modified Eagle medium (DMEM), both supplemented with 10% fetal bovine serum (FBS) and 1% Penicillin−Streptomycin. All cell culture reagents were from Gibco (Grand Island, NY, USA). Cells were cultured in a humidified atmosphere with 5% CO_2 at 37 °C. Female 6-week-old BALB/c mice were purchased from GemPharmaTech (Nanjing, China) and housed in the specific pathogen-free (SPF) facility of the University of Electronic Science and Technology of China (UESTC). All *in vivo* procedures were performed under anesthesia, and animal experiments followed the guidelines of the Institutional Animal Care and Ethics Committee of UESTC (Approval Number: 1061420210305001).

2.3. Characterization and apparatus

The particle size and zeta potential were measured by Zetasizer nanoseries (Malvern Instruments, Nano ZS90, Malvern, UK). The absorbance of samples was measured by the ultraviolet-visible spectrometer (Hitachi, UV-2910, Tokyo, Japan). The transmission electron microscope (JEOL Ltd., JEM-100CX, Tokyo, Japan) and the scanning electron microscope (JEOL Ltd., JSM-6490LV, Tokyo, Japan) were applied to observe the morphology and structure of samples. The infrared absorption bands were detected by the Fourier transform infrared spectrometer (Thermo Fisher Scientific, Nicolet iS5, Waltham, MA, USA). The crystal structures were studied by the X-ray diffractometer (PANalytical, X'Pert Pro MPD, Almelo, Netherlands). The absorbance of microplates was measured by the multifunctional microplate reader (BioTek Instruments, ELx808, Winooski, VT, USA). Pore size distribution and nitrogen adsorption−desorption isotherm were determined by the Brunauer-Emmett-Teller (BET) analyzer (Micromeritics, ASAP 2020, Norcross, GA, USA). Near-infrared (NIR) irradiation was provided by the 808 nm laser (BWT, K808F14CC, Beijing, China). The temperature change was probed by thermocouples (Omega Engineering, HH806AU, Stamford, CT, USA). Photothermal images were captured by the infrared thermal camera (FLIR, E54 Series, Wilsonville, OR, USA). Fluorescence images were acquired by the inverted fluorescence microscope (Nikon, TE2000-U, Tokyo, Japan) or the confocal laser scanning microscope (CLSM) (Carl Zeiss, LSM-800, Jena, Germany). Living fluorescence imaging was conducted using an *in vivo* imaging system (PerkinElmer, IVIS Lumina Series III, Waltham, MA, USA). Flow cytometric data were collected by the flow cytometer (Agilent, NovoCyte Quanteon, Santa Clara, CA, USA) and were analyzed using the FlowJo software (FlowJo LLC, FlowJo version 10.8.1, Ashland, OR, USA).

2.4. Preparation of CRPO/G@ALG

For the synthesis of CuS, 480 mg of PVP-K30 was added to a flask along with 50 mL of ultrapure water and stirred until dissolved. Subsequently, $CuCl_2$ solution (0.5 mol/L, 200 μL) was introduced, followed by 5 min of stirring. Next, NaOH solution (0.1 mol/L, 50 mL) and hydrazine hydrate (85.0%, 16 μL) were added successively, and the mixture was vigorously stirred for 5 min. Then, Na_2S solution (4 mol/L, 400 μL) was incorporated. The flask was placed in a water bath at 60 °C and stirred at 500 rpm for 2 h (Zhengzhou Greatwall Scientific Industrial and Trade Co., Ltd., Zhengzhou, China). The products were collected by centrifugation at 11,000 rpm for 10 min (Eppendorf, 5804R, Hamburg, Germany), washed three times with ultrapure water, and dried to obtain CuS.

For the preparation of CRPO, 15 mg of CuS and 3 mg of R848 were dispersed in 15 mL of a methanol-water mixture (1:1, *v*/*v*), followed by sonication for dispersion and stirring at room temperature for 24 h. The product was collected by centrifugation and washed three times with methanol to obtain CuS@R. Subsequently, 15 mg of CuS@R and 50 mg of PEI were dispersed in 15 mL of ultrapure water, followed by sonication for dispersion. The pH of the mixed solution was adjusted to pH 7.4 using 0.1 mol/L dilute hydrochloric acid and stirred at room temperature for 24 h. The product was collected by centrifugation and washed three times with ultrapure water to obtain CuS@RP (CRP). Next, 15 mg of CRP was dissolved in 15 mL of ultrapure water, and 15 mg of OVA was added. The mixture was sonicated and then stirred at room temperature for 2 h. The product was collected by centrifugation, washed three times with ultrapure water, and obtained CRPO. Near-infrared dye-labeled material CIPO for *in vivo* imaging followed the same procedure, except that R848 was replaced with ICG.

For the fabrication of CRPO/G@ALG, 100 mg of ALG, 2 mg of CRPO, and 0.1 mg of GM-CSF were dispersed in 10 mL of ultrapure water and stirred until fully dissolved, yielding CRPO/G@ALG in the sol phase. CRPO/G@ALG was transferred to a dialysis bag (MW = 100 kDa), placed in $CaCl_2$ solution (1.8 mmol/L) that mimicked physiological conditions, and stirred overnight to obtain CRPO/G@ALG in the gel phase. CuS@ALG, CRPO@ALG, and G@ALG were prepared in a similar manner.

2.5. Gelation and degradation evaluation

To assess the gelation behavior of CRPO/G@ALG *in vitro*, sol-phase ALG and CRPO/G@ALG ([ALG] = 10 mg/mL, [CuS] = 200 μg/mL, [GM-CSF] = 10 μg/mL) were prepared, placed in dialysis bags (MW = 100 kDa), and immersed in 500 mL of PBS containing 1.8 mmol/L $CaCl_2$. The mixture was gently stirred overnight until complete gelation. The rheological properties of both hydrogels were analyzed using a rotational rheometer (Thermo Fisher Scientific, HAAKE MARS 60, Waltham, MA, USA), measuring the storage modulus (G') and loss modulus (G'') at room temperature with an angular frequency range of 1 to 100 rad/s and a constant strain of 1%.

To investigate the gelation and degradation of CRPO/G@ALG *in vivo*, sol-phase CRPO/G@ALG ([ALG] = 10 mg/mL, [CuS] = 30 mg/kg, [GM-CSF] = 10 μg/mL) was prepared as described. A total of 100 μL of CRPO/G@ALG was subcutaneously injected into the right hind limb of BALB/c female mice. Mice were euthanized at designated time points (Days 1, 7, 14, and 28). Gelation and degradation of the hydrogel at the injection site were observed, and the degradation rate was evaluated by recording the remaining hydrogel mass.

2.6. Immunogenic cell death measurement

For calreticulin (CRT) exposure, 4T1 cells (2×10^5 cells/well) were seeded into culture dishes and incubated overnight. The medium was replaced with 1640 medium containing CuS, CRP, or CRPO, and the cells were incubated for 8 h. Non-internalized nanoparticles were removed, and fresh medium was added. The laser-treated group was exposed to an 808-nm laser (1.0 W/cm^2, 5 min). After an additional 24 h incubation, cells were fixed with 4% paraformaldehyde, blocked with 1% bovine serum albumin (BSA), and incubated overnight with calreticulin antibody (1:400). Subsequently, the cells were incubated with Alexa 488-labeled secondary antibody (1:400) for 2 h, followed by DAPI staining for 20 min. CRT exposure was visualized using CLSM (Carl Zeiss).

For high-mobility group box 1 (HMGB1) release, 4T1 cells (5×10^5 cells/well) were seeded in 6-well plates and incubated overnight. The same treatment as for CRT exposure was applied. The culture supernatant was collected and centrifuged at $1500 \times g$ for 3 min (Eppendorf), and the pellet was discarded. The content of HMGB1 in the supernatant was then detected using an HMGB1 ELISA kit following the manufacturer's protocol.

2.7. DC recruitment and maturation investigation

For DC recruitment, DC 2.4 cells (3×10^6 cells/well) were seeded into the upper chambers of Transwell systems (24-well plates, 8 μm pore size) and incubated for 4 h. Subsequently, 100 μL of CRPO@ALG or CRPO/G@ALG hydrogel ([ALG] = 10 mg/mL, [GM-CSF] = 10 μg/mL) was added to the lower chambers, followed by the addition of the appropriate medium. The plates were then returned to the incubator for 24 h. After incubation, non-migratory cells in the upper chambers were removed. The inserts were fixed with 4% paraformaldehyde at room temperature for 30 min, followed by staining with anti-CD11c-FITC and DAPI for 30 min. Finally, the inserts were placed on glass slides, and the number of migrating DC cells in the lower chambers was observed using an inverted fluorescence microscope (Nikon).

For DC recruitment, 4T1 cells (2×10^4 cells/well) were seeded into the upper chambers of Transwell systems and incubated for 24 h. Subsequently, 100 μL of G@ALG, CuS@ALG, CRPO@ALG, or CRPO/G@ALG hydrogel ([CuS] = 200 μg/mL, [ALG] = 10 mg/mL, [GM-CSF] = 10 μg/mL) was applied to the upper chambers, followed by an additional 24 h incubation. In the laser treatment group, the cells were irradiated with an 808 nm laser (1.0 W/cm^2, 5 min). Subsequently, DC cells (5×10^5 cells/well) were seeded into the lower chambers and co-cultured with the pre-treated 4T1 cells for 24 h. Upon completion of the co-culture, the supernatant from the co-culture system and the DC cells in the lower chambers were collected. The levels of cytokines TNF-α and IL-6 in the supernatant were quantified using ELISA kits. The DC cells were then stained with a panel of antibodies (anti-CD11c-FITC, anti-CD80-APC, and anti-CD86-PE) for 30 min. After three washes with PBS, the frequency of matured DC cells was evaluated by flow cytometry (Agilent).

2.8. Tumor model and treatment regimen

To establish the bilateral 4T1 tumor-bearing mouse model, 100 μL of 4T1 cell suspension (1×10^7 cells/mL) was subcutaneously injected into the right hind limb of BALB/c female mice, inducing the primary tumor on the right flank. Following a 5-day incubation period, a second dose of 100 μL of 4T1 cell suspension (2×10^6 cells/mL) was administered subcutaneously into the left hind limb to form the distal tumor on the left flank. Once the primary tumor reaches approximately 100 mm^3 in volume, mice are randomly assigned to five groups: ALG, CRPO@ALG, CuS@ALG + L, CRPO@ALG + L, and CRPO/G@ALG + L. Peritumoral injections of ALG, CRPO@ALG, CuS@ALG, or CRPO/G@ALG (100 μL, [ALG] = 10 mg/mL, [CuS] = 15 mg/kg, [GM-CSF] = 10 μg/mL) are administered at the primary tumor sites. For the laser-treated groups, tumors receive 808 nm laser irradiation (1 W/cm^2, 5 min) on Days 1, 3, and 5. Throughout the 15-day treatment period, body weight and tumor volume were monitored every two days, and tumor volume was calculated following the formula, as shown in Eq. (1):

$$V = L \times S^2/2 \tag{1}$$

where L is the longer diameter, and S is the shorter diameter.

At the end of the treatment, mice are euthanized, and tumors and major organs are harvested for subsequent histological and immunological analyses. The tumor inhibition rate (TIR) was calculated using the following formula, as shown in Eq. (2):

$$\text{TIR}\ (\%) = (V_{\text{control}} - V_{\text{treatment}})/V_{\text{control}} \times 100 \tag{2}$$

where V_{control} and $V_{\text{treatment}}$ represent the final tumor volume of mice in the control and treatment groups.

For the lung metastasis model, 100 μL of 4T1 cell suspension (1×10^7 cells/mL) was subcutaneously injected into the right hind limb of BALB/c female mice to establish the primary tumor. After 6 days, a second dose of 100 μL of 4T1 cell suspension (2×10^6 cells/mL) was administered intravenously *via* the tail vein to induce lung metastasis. Once the primary tumor reaches approximately 100 mm^3 in volume, mice are randomly assigned into three groups: ALG, CRPO/G@ALG, and CRPO/G@ALG + L. Peritumoral injections of 100 μL ALG or CRPO/G@ALG ([ALG] = 10 mg/mL, [CuS] = 15 mg/kg, [GM-CSF] = 10 μg/mL) are administered at the primary tumor sites. On Days 1, 3, and 5, tumors in the laser-treated groups are irradiated with an 808 nm laser (1 W/cm^2, 5 min). At the end of the treatment, mice are euthanized, and the lung and spleen tissues are harvested for subsequent histological and immunological analyses.

2.9. Histological and immunological staining

ICD induction and DC recruitment in tumors were visualized by CRT and CD11 immunofluorescence staining. Three days after finishing the therapeutic intervention, primary tumors from each group were collected, fixed in 10% formalin, then embedded in paraffin and sectioned. The tumor sections were stained, and fluorescent images were captured using an inverted fluorescence microscope (Nikon). For antitumor efficacy evaluation, on Day 15 of treatment, both primary and distant tumors from each group were collected for hematoxylin-eosin (HE), Ki67, Granzyme B, and TUNEL staining. To evaluate immune cell infiltration in distant tumors, distant tumors from each group were collected on Day 15 of treatment, and CD8, CD4, and Foxp3 staining were performed. The lung metastasis tumor-bearing mice were sacrificed on Day 21, and the lungs were harvested and fixed overnight in Bouin's solution to identify metastatic nodules. The number of

pulmonary metastases was quantified and analyzed. Lung tissues were further processed for HE, Ki67, and CD8 staining.

2.10. Flow cytometry and cytokine detection

Single-cell suspensions were prepared from the primary tumors, tumor-draining lymph nodes (TDLNs), and spleens of mice subjected to different treatments. Flow cytometry was performed to analyze immune cell populations and activation states. For dendritic cell (DC) recruitment and migration, on Day 8, primary tumor cell suspensions were stained with flow cytometry antibodies: anti-CD11c-FITC, anti-CD103-APC, and anti-CCR7-PE. On the same day, TDLN cell suspensions were stained with antibodies for DC maturation: anti-CD11c-FITC, anti-CD86-APC, and anti-CD80-PE. Serum was collected on Day 8 for cytokine detection, including TNF-α, IFN-γ, IL-6, and IL-10, measured using ELISA kits. On Day 15, the cell suspensions from primary tumors or spleens were stained with flow cytometry antibodies: anti-CD3-FITC, anti-CD4-APC, anti-CD8-APC 780, and anti-Foxp3-PE for phenotypic analysis of T cells. On Day 21, spleen cell suspensions were analyzed for memory T cells by staining with anti-CD3-FITC, anti-CD8-APC-780, anti-CD44-APC, and anti-CD62L-PE antibodies.

2.11. Statistical analysis

Data are presented as the mean ± standard deviation (SD) using GraphPad Prism software version 10 (GraphPad Software Inc., San Diego, CA, USA). The corresponding figure legends provided the sample sizes (n) for statistical calculations. The two-tailed unpaired Student's t-test was applied to compare the two groups. One-way analysis of variance (ANOVA) followed by Tukey's *post hoc* test was used for analysis among multiple groups. Statistical significance was indicated as not significant (ns) for $P > 0.05$, $*P < 0.05$, $**P < 0.01$, $***P < 0.001$, and $****P < 0.0001$. More experimental methods are available in the Supporting Information

3. Results and discussion

3.1. Preparation and characterization of nanovaccine CRPO

Initially, CuS was synthesized using a one-step hydrothermal method. Transmission electron microscopy (TEM) imaging and nitrogen adsorption-desorption analysis confirmed the hollow mesoporous structure of CuS, with an average particle size of 146.2 ± 8.4 nm and a pore size of 2.7 nm (Supporting Information Fig. S1A and S1B). The X-ray diffraction (XRD) pattern of the synthesized sample depicted in Fig. S1C closely matched the standard diffraction peaks of CuS (JCPDS No. 01-1281), further verifying the successful synthesis of hollow mesoporous CuS.

Subsequently, CuS@RPO (denoted as CRPO) was obtained through a stepwise process involving immune agonist incorporation, surface functionalization, and model antigen adsorption based on CuS. Variations in particle size and zeta potential preliminarily validated the success of each preparation stage (Supporting Information Fig. S2A). Negligible changes in particle size indicated that CRPO remained relatively stable in various dispersion media for at least one week (Fig. S2B). The TEM image in Fig. 1A displays that CRPO maintained a uniformly dispersed spherical morphology, similar to the original particles, with a slight increase in particle size to 154.7 ± 9.6 nm. The TEM-EDS mapping image visualized the existence and distribution of the elements copper (Cu), sulfur (S), nitrogen (N), and oxygen (O) in CRPO (Fig. 1B). Moreover, the ultraviolet-visible (UV−Vis) absorption and Fourier transform infrared (FTIR) spectra shown in Fig. 1C and D exhibit the relevant characteristic peaks of R848 and OVA. These results provide ample evidence supporting the successful fabrication of CRPO.

CRPO was designed as a photoimmunological nanovaccine, uniquely integrating excellent photothermal properties with the capacity to serve as an immune stimulator. To evaluate its potential for hyperthermia-driven immunogenic cell death (ICD), the photothermal performance of CRPO was investigated *in vitro*. The photothermal heating curves of CRPO showed a significant dose-dependent and power-density-dependent temperature increase under near-infrared (NIR) laser irradiation (Fig. 1E and F). Thermal infrared images revealed that the temperature of the CRPO solution (200 μg/mL) rose to 62.8 °C after 5 min of irradiation (808 nm, 1.0 W/cm^2), while PBS illustrated negligible thermal changes under identical conditions (Fig. 1G). Moreover, no significant photothermal attenuation was observed during four successive heating and cooling cycles (Fig. 1H). These findings evidence the exceptional photothermal conversion capability and stability of CRPO, positioning it as a promising candidate for ICD induction and supporting photothermal immunotherapy applications.

The *in vitro* drug release behavior of CRPO was further investigated under simulated local acidity and irradiation conditions at the tumor site, using R848 as the representative drug (Fig. 1I). Under acidic conditions (pH 5.5), drug release was significantly higher than at physiological pH (7.4), attributed to the protonation of the amino group of PEI. This protonation leads to the expansion of the molecular chain and enhanced electrostatic repulsion, which facilitates drug release[40,41]. Furthermore, NIR irradiation triggered pulsatile and abrupt drug liberation due to the photothermal effect, which temporarily raised the temperature and accelerated molecular diffusion. Notably, the highest cumulative drug discharge occurred when both the photothermal effect and acidic conditions were present simultaneously, with approximately 63.0% of R848 released over 24 h. These observations disclosed the pH-responsive and NIR-triggered release properties of CRPO, which enable controlled drug delivery, potentially improving payload bioavailability and therapeutic efficacy.

3.2. Intracellular fate and immunogenic cell death induction of CRPO

The biocompatibility of CRPO was estimated to ensure its suitability for biological applications (Supporting Information Fig. S3). The cell viability of 4T1, EMT-6, and NIH-3T3 cells was over 75% after incubation with CRPO at concentrations up to 400 μg/mL, demonstrating excellent biocompatibility in both tumor and normal cell lines. This high level of biocompatibility fulfills a key prerequisite for clinical translation. Upon NIR laser irradiation, cell viability decreased dramatically in a dose-dependent manner, underscoring the favorable photothermal effect and effective phototoxicity of CRPO at the cellular level.

Inadequate internalization and lysosomal trapping of nanomedicine in tumor cells greatly limit therapeutic efficacy[42-44]. To track the intracellular fate of CRPO, the fluorescence-labeled CRPO-FITC was employed to investigate the cellular uptake and lysosomal escape behavior in 4T1 cells at different time intervals. Confocal images in Fig. 2A reveal that the green

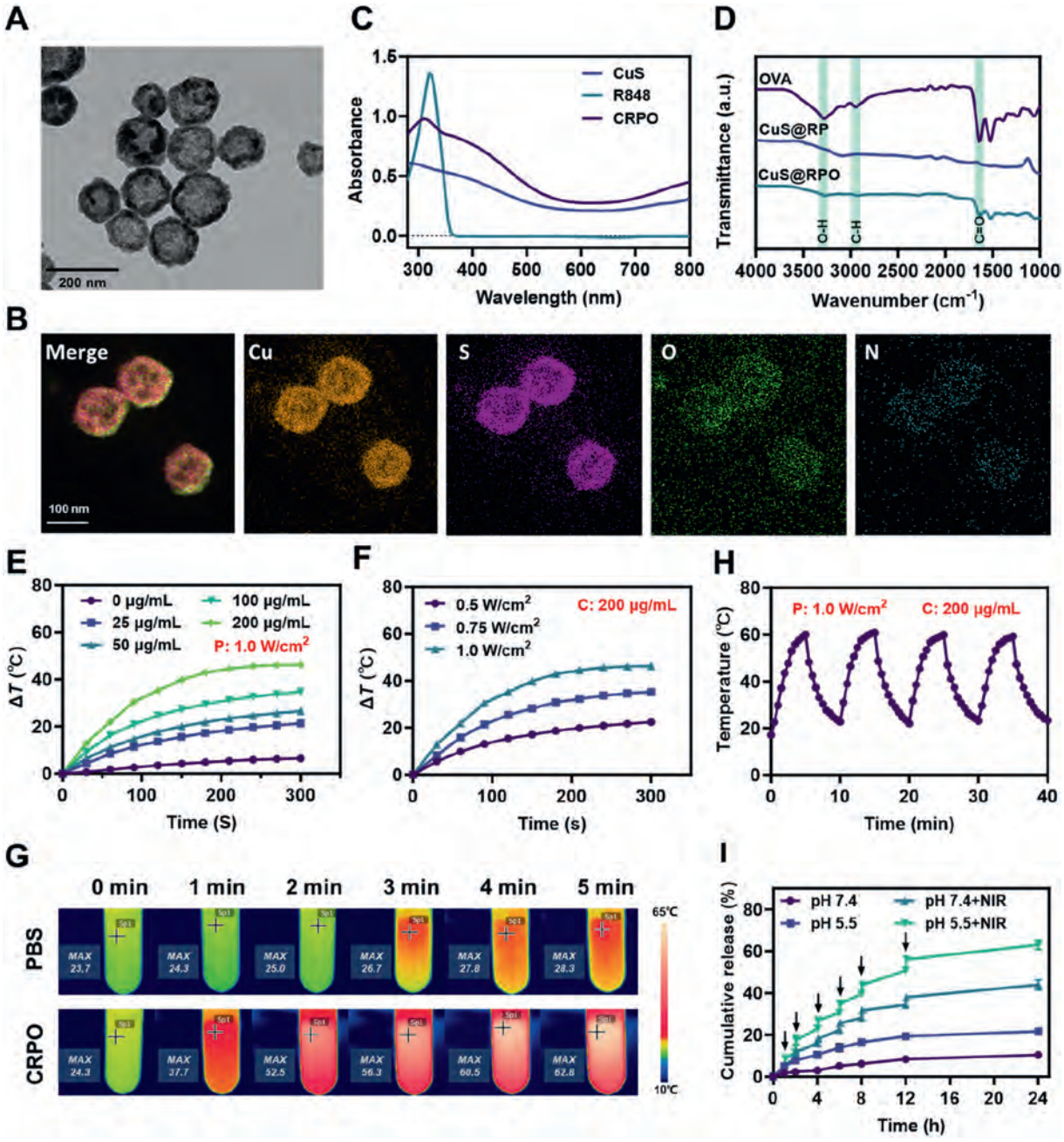

Figure 1 Characterization of nanovaccine CRPO. (A) The TEM image of CRPO. (B) The TEM-EDX mapping image of CRPO. (C) The UV−Vis spectra of CRPO. (D) The FTIR spectra of CRPO. The photothermal heating curves of CRPO aqueous solution upon NIR laser irradiation (E) at different concentrations and (F) under various power densities. (G) The corresponding thermal images of PBS or CRPO. (H) The photothermal stability of CRPO during four on/off NIR laser irradiation cycles. (I) The cumulative release profile of R848 in CRPO at different pH values with or without NIR laser irradiation. Black arrows indicate NIR laser irradiation for 5 min.

fluorescence progressively increased and was predominantly distributed in the cytoplasm, indicating the cumulative internalization of CRPO-FITC into cells over time. The lysosomal trapping represents a primary obstacle to therapeutic delivery, and lysosome escape is critical for protecting payloads from undesirable degradation[45,46]. Therefore, the lysosomal escape capability of CRPO-FITC was further examined (Fig. 2B). After incubation for 6 h, green fluorescence (CRPO-FITC) almost overlapped with red fluorescence (Lyso Tracker), resulting in widespread yellow fluorescence in the merged image, confirming high colocalization of CRPO-FITC and lysosomes. However, a remarkable separation of green fluorescence and a pronounced disappearance of red fluorescence was observed when the incubation time was extended to 12 h, implying lysosomal rupture and CRPO-FITC liberation. These findings testify that CRPO achieves efficient cellular uptake and rapid lysosomal escape, avoiding premature degradation of the payload, especially for bioactive cargo, which lays a solid foundation for subsequent satisfactory treatment outcomes.

To comprehensively investigate the cell death patterns induced by various formulations in 4T1 cells, a series of assays, including

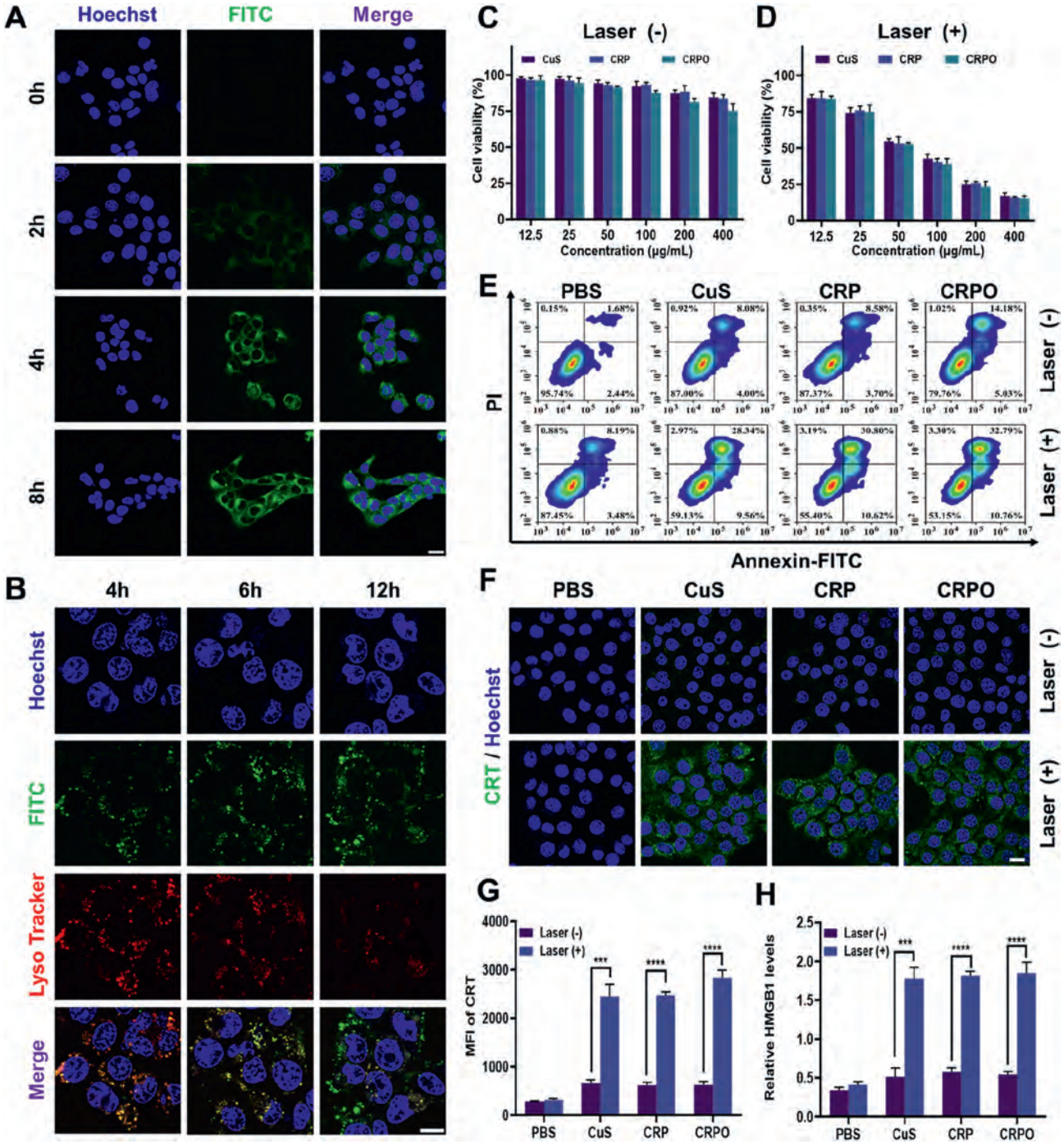

Figure 2 Cellular uptake and immunogenic cell death induction of CRPO. (A) The cellular uptake and (B) The intracellular distribution of CRPO in 4T1 cells with time duration. Scale bar: 20 μm. (C, D) Cell viability of 4T1 cells after treatment with different formulations in the absence or presence of NIR laser irradiation. (E) Apoptosis flow cytometry analysis of 4T1 cells after various treatments. (F) Immunofluorescent images of CRT in 4T1 cells after various treatments. Scale bar: 40 μm. (G) The quantitative analysis of the mean fluorescence intensity of CRT. (H) The level of HMGB1 in the culture supernatants of 4T1 cells after various treatments. The data are presented as mean ± SD ($n = 3$), and statistical significance was calculated by one-way analysis of variance (ANOVA), $^{***}P < 0.001$, and $^{****}P < 0.0001$.

CCK-8 assay, live/dead cell staining, and cell apoptosis analysis, were carried out in sequence. As shown in Fig. 2C and D, CuS, CuS@R, and CRPO exhibited marginal cytotoxicity without NIR laser irradiation, highlighting the low intrinsic cytotoxicity of these formulations. Conversely, considerable cell death was identified in all groups treated with the aforementioned formulations upon NIR laser irradiation. Thus, this NIR-triggered cell death may result from thermal damage induced by the photothermal effect of these formulations. Calcein-AM/PI staining images intuitively illustrated extensive cell death, with nearly all cells exhibiting red fluorescence at a working concentration of 200 μg/mL, indicating overwhelming cytotoxicity under

irradiation (Supporting Information Fig. S4). Although higher-dose formulations led to more intense tumor cell killing, severe hyperthermia caused massive necrosis, triggering excessive inflammation and impairing ICD induction, ultimately compromising subsequent immune activation[47-49]. Considering the sustained release properties of the hydrogel system and the need to minimize negative impacts on immune responses, further investigations were carried out at a lower dose of 100 μg/mL. The representative plots from Annexin V-FITC/PI-based flow cytometry apoptosis assays, depicted in Fig. 2E, reveal a prominent increase in apoptotic cells rather than fierce necrosis across all formulations upon irradiation. These results suggest that by optimizing the administration dosage, CRPO can achieve a relatively mild photothermal effect, preventing tumor antigen disruption from high temperatures. This strategy strikes a desirable balance between efficient tumor cell destruction and sufficient tumor immunogenicity improvement.

Photothermally induced immunogenic cell death is a well-established mechanism that offers a spatiotemporally controllable approach to creating an *in situ* antigen reservoir, thereby initiating a cascade of immune responses[15,50,51]. The exposure of tumor-associated antigens (TAAs) and damage-associated molecular patterns (DAMPs) constitutes a hallmark of ICD[52,53]. To examine ICD induction following various treatments, calreticulin (CRT) exposure and high mobility group box 1(HMGB1) release were evaluated as representative biomarkers. Immunofluorescence images and corresponding quantitative fluorescence intensity analysis illustrated widespread and intense CRT signals (green fluorescence) in NIR laser-treated groups, except for the PBS control, indicating abundant CRT translocation to the cell surface (Fig. 2F and G). Likewise, extracellular HMGB1 levels were substantially elevated in samples treated with CuS, CuS@R, or CRPO combined with NIR laser irradiation (Fig. 2H). These observations demonstrated that CRPO effectively induced ICD, facilitating tumor cell elimination and enhancing tumor immunogenicity to stimulate downstream antitumor immune responses.

3.3. Preparation and characterization of hydrogel vaccine CRPO/G@ALG

In the burgeoning field of tumor vaccine innovation, nanocomposite-based hydrogel vaccines have emerged as a transformative platform by integrating the advantages of hydrogel and nanovaccines[31,37,38]. Spurred by the latest advances in hydrogel vaccines, an exploration was initiated to ascertain the feasibility of co-encapsulating the nanovaccine CRPO and the DC recruitment factor GM-CSF within an alginate hydrogel to engineer the photoimmunological hydrogel vaccine CRPO/G@ALG. To investigate the gelation behavior of CRPO/G@ALG *in vitro*, studies were conducted to mimic the physiological concentration of calcium ions. As expected, the addition of calcium chloride ($CaCl_2$) solution triggered a sol-gel transition of CRPO/G@ALG (Fig. 3A). To further explore the hydrogel properties, the storage modulus (G') and the loss modulus (G'') of ALG and CRPO/G@ALG were measured using a rotational rheometer (Fig. 3B). Notably, in both the ALG and CRPO/G@ALG, G' was substantially higher than G'', confirming their ability to form stable hydrogels in response to physiological calcium ions. SEM images of ALG and CRPO/G@ALG hydrogels were showcased in Fig. 3C and D, revealing that the internal porous three-dimensional structure was discernible in the cross-section of both lyophilized hydrogels. Particularly, CRPO/G@ALG displayed a rougher surface compared to ALG, suggesting the success of hydrogel fabrication and payload integration. Next, to assess the *in vitro* drug liberation profile of the CRPO/G@ALG hydrogel, the cumulative release of GM-CSF was monitored (Supporting Information Fig. S5). Approximately 40% of GM-CSF was released from the hydrogel within 7 days, indicating that the gelation of CRPO/G@ALG may offer a prolonged and controlled payload supply. This property potentially enhances the therapeutic efficacy and reduces the medication frequency in biomedical applications.

Tumor-driven immunosuppression severely impairs DC infiltration and maturation within the tumor microenvironment, disrupting the capture and presentation of tumor antigens and consequently hindering the initiation of effective antitumor immune responses[21,54,55]. To elucidate the immunological potential of CRPO/G@ALG, its ability to stimulate DC recruitment and maturation was investigated *in vitro* using a Transwell co-culture system (Fig. 3E). Immunofluorescence images revealed a sparse distribution of DCs in the CRPO@ALG group, whereas the CRPO/G@ALG group demonstrated significantly enhanced DC accumulation, demonstrating the superior recruitment capacity stemming from the inclusion of GM-CSF (Fig. 3F). Representative flow cytometry plots and statistical data indicated varying degrees of DC maturation across G@ALG, CuS@ALG + L, CRPO@ALG, and CRPO@ALG + L groups, with the photothermal effect contributing most prominently (Fig. 3G and H). Among these, CRPO/G@ALG witnessed the highest proportion of DC maturation, emphasizing the synergistic effects of the nanovaccine, photothermal properties, and GM-CSF in overcoming intrinsic tumor immunosuppression and amplifying immune activation. Correspondingly, culture supernatants were collected to determine cytokine secretion levels (Fig. 3I and J). The CRPO/G@ALG group exhibited significantly elevated levels of pro-inflammatory cytokines, including tumor necrosis factor-alpha (TNF-α) and interleukin-6 (IL-6), providing additional evidence of the most robust DC maturation. These results highlight the potential of CRPO/G@ALG as a versatile formulation for enhancing adaptive immunity by promoting DC recruitment, maturation, and cytokine production.

3.4. In vitro photothermal and sustained release properties evaluation

The encouraging *in vitro* experimental results prompted further investigation of the *in vivo* properties of CRPO/G@ALG. The photothermal performance of CRPO/G@ALG was first evaluated using an infrared thermal camera to monitor temperature changes at the tumor site in 4T1 subcutaneous tumor-bearing mice (Fig. 4A and C). The ALG group showed minimal temperature alterations, while the CRPO@ALG group exhibited a significant temperature increase under NIR irradiation at the tumor site. Remarkably, the tumor site temperature rose to approximately 45 °C in about 2 min, a level sufficient to achieve effective photothermal therapy. This observation confirms that the incorporation of CRPO imparts excellent photothermal properties to the hydrogel CRPO@ALG. Afterward, the *in vivo* gelation and degradation behavior of CRPO/G@ALG was assessed by determining the residual hydrogel after subcutaneous implantation (Fig. 4B and D). Representative images of the subcutaneous injection sites demonstrated that CRPO/G@ALG transitioned into a gel phase on the first day after injection. The hydrogel gradually degraded over time, with approximately 30% of the hydrogel

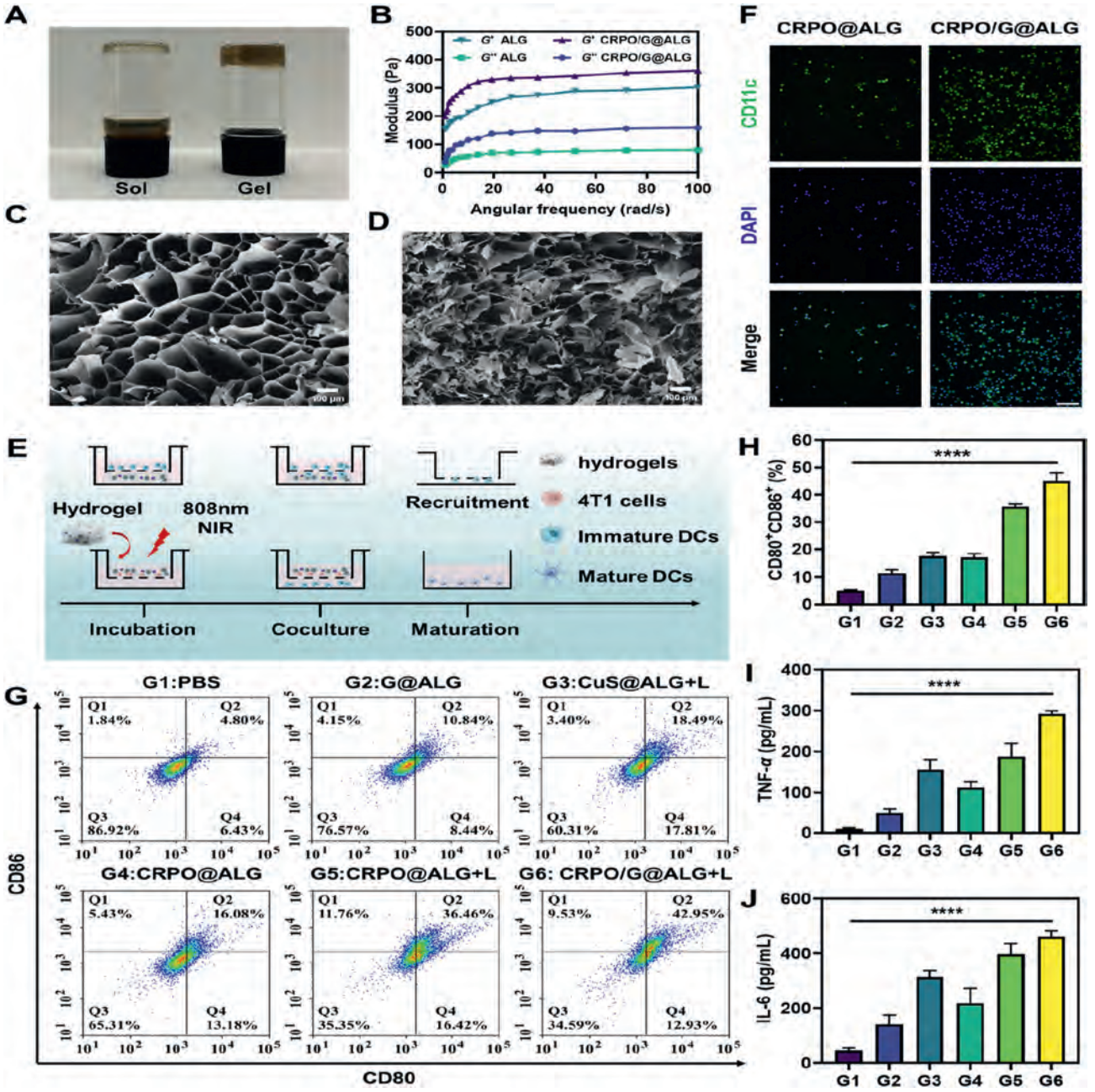

Figure 3 Characterization of hydrogel vaccine CRPO/G@ALG. (A) The sol-gel phase transition behavior of CRPO/G@ALG. (B) The rheological analysis of ALG and CRPO/G@ALG after complete gelation. The measurement of the energy storage modulus (G′) and loss modulus (G″) under room temperature with an angular frequency varying from 1 to 100 rad/s at a constant strain of 1%. (C, D) The SEM micrographs of ALG and CRPO/G@ALG hydrogels. (E) Schematic illustration of DC recruitment and maturation assay *in vitro*. (F) Representative immunofluorescence staining images of the DC recruitment assay. Scale bar: 100 μm. (G, H) Representative flow cytometry plots and statistical analysis of the proportion of mature DCs ($CD86^+CD80^+$) after various treatments. (I, J) The cytokine secretion levels of TNF-α and IL-6 in the coculture supernatant. The data are presented as mean ± SD ($n = 3$), and statistical significance was calculated by one-way analysis of variance (ANOVA), $^{****}P < 0.0001$.

remaining on Day 28. These data demonstrate the successful gelation and prolonged degradation profile of CRPO/G@ALG *in vivo*, supporting its potential for precise and sustained payload delivery.

Subsequently, to further estimate the *in vivo* sustained release properties of the hydrogel, the near-infrared fluorescent dye ICG was adopted to replace R848, fabricating ICG-labeled nanovaccine CIPO and CIPO@ALG. The biodistribution of the nanovaccine was investigated using a live imaging system. The hydrogel system substantially extended the retention time of the nanovaccine at the injection site, with distinct fluorescence signals persisting for up to 14 days post-injection (Fig. 4E and Supporting Information Fig. S6A). Inversely, the free CIPO group exhibited rapid clearance, in which fluorescence signals declined sharply on

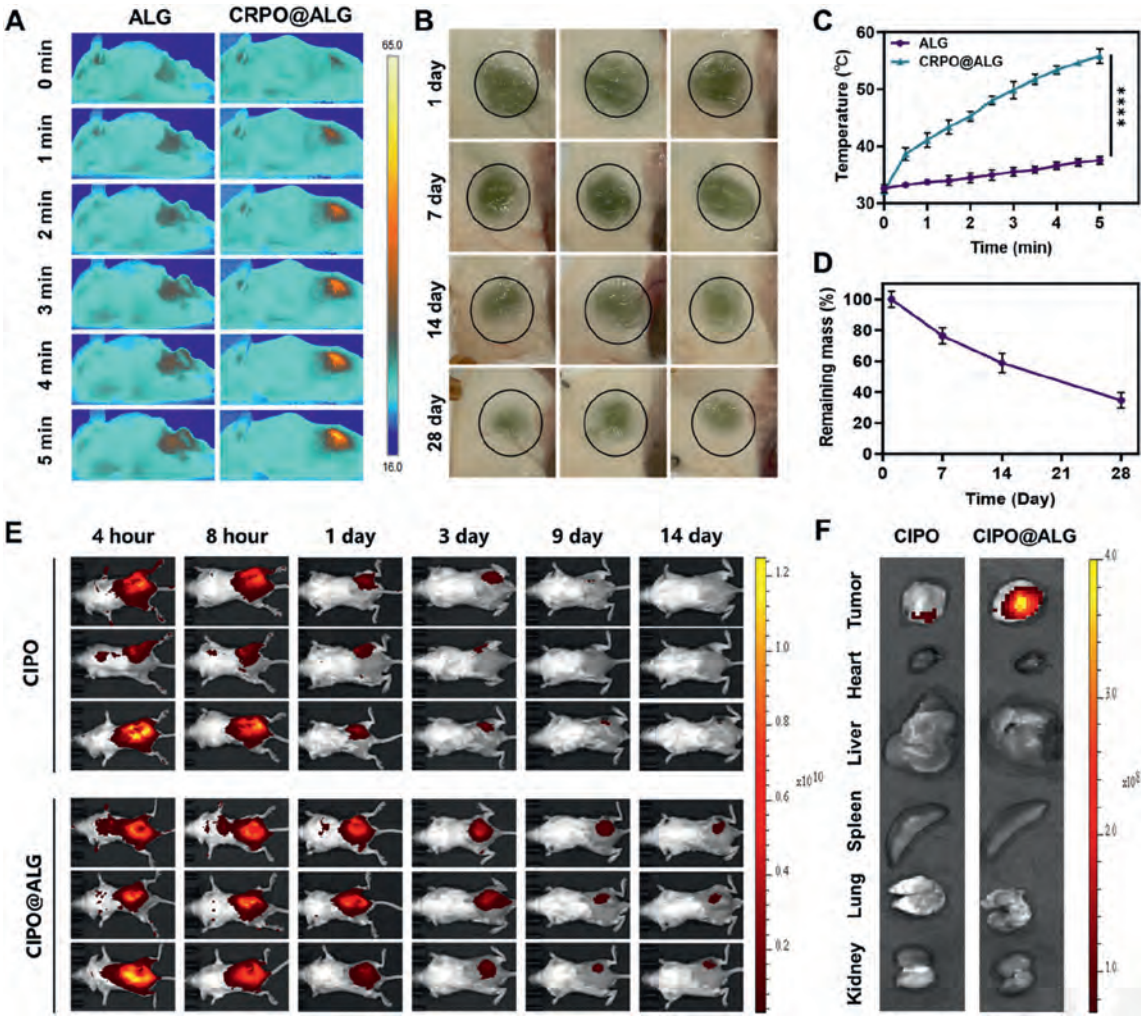

Figure 4 *In vivo* photothermal and sustained release properties. (A) Representative thermographic images of 4T1 subcutaneous tumor-bearing mice after peritumoral injection of ALG or CRPO @ALG with NIR laser irradiation. (B) The gelation and degradation performance of CRPO/G@ALG after subcutaneous implantation over 28 days. (C) Quantification analysis of the temperature in the tumor region (D) Quantification analysis of the remaining mass of CRPO/G@ALG hydrogel after subcutaneous implantation. (E) The near-infrared fluorescence imaging of 4T1 tumor-bearing mice after peritumoral injection of CIPO or CIPO@ALG over 14 days. (F) Representative ex vivo near-infrared fluorescence images of major organs and tumor tissues on the 14th day post-injection. The data are presented as mean ± SD ($n = 3$), and statistical significance was calculated by one-way analysis of variance (ANOVA), $^{****}P < 0.0001$.

the first day and became nearly undetectable by Day 9. Notably, *ex vivo* imaging of major organs and tumors on Day 14 revealed obvious fluorescence signals exclusively at the tumor site in the CIPO@ALG hydrogel group (Fig. 4F and Fig. S6B). These findings validate that the CIPO@ALG hydrogel effectively retains payloads at the tumor site, minimizes diffusion to off-target tissues, and underscores its crucial contribution to localized retention and sustained drug release.

3.5. In vivo antitumor therapeutic efficacy assessment

The antitumor activity of CRPO/G@ALG was evaluated in a bilateral subcutaneous 4T1 tumor-bearing mouse model (Fig. 5A). The tumor growth curves in Fig. 5B and C describe the progression of primary and distant tumors. In the ALG group, both primary and distant tumors exhibited rapid growth, indicating that ALG has negligible efficacy in preventing tumor progression. The CRPO@ALG and the CuS@ALG plus irradiation groups, representing the immune stimulation alone and ICD induction alone treatments, respectively, showed moderate tumor suppression on both sides of the tumors. The CRPO@ALG with irradiation group, combining immune stimulation and ICD induction, demonstrated more effective tumor arrest. Notably, the CRPO/G@ALG with irradiation group achieved the most prominent tumor inhibition. The tumor inhibition rates of this group reached 92.4% at the primary site and 71.2% at the distant site (Supporting Information Fig. S7A and S7B). The weight and digital photo of tumors confirmed that this group exhibited the smallest tumor masses and the lightest tumor weights Fig. 5D–G. The pronounced therapeutic efficacy of the CRPO@ALG with irradiation group is attributed to the synergy of immune stimulation, ICD induction, and DC recruitment, which collectively enhanced tumor antigen presentation and boosted antitumor immunity.

Moreover, histological and immunological staining were performed to further assess the treatment outcomes of different groups, including HE, Ki67, Granzyme B, and TUNEL staining

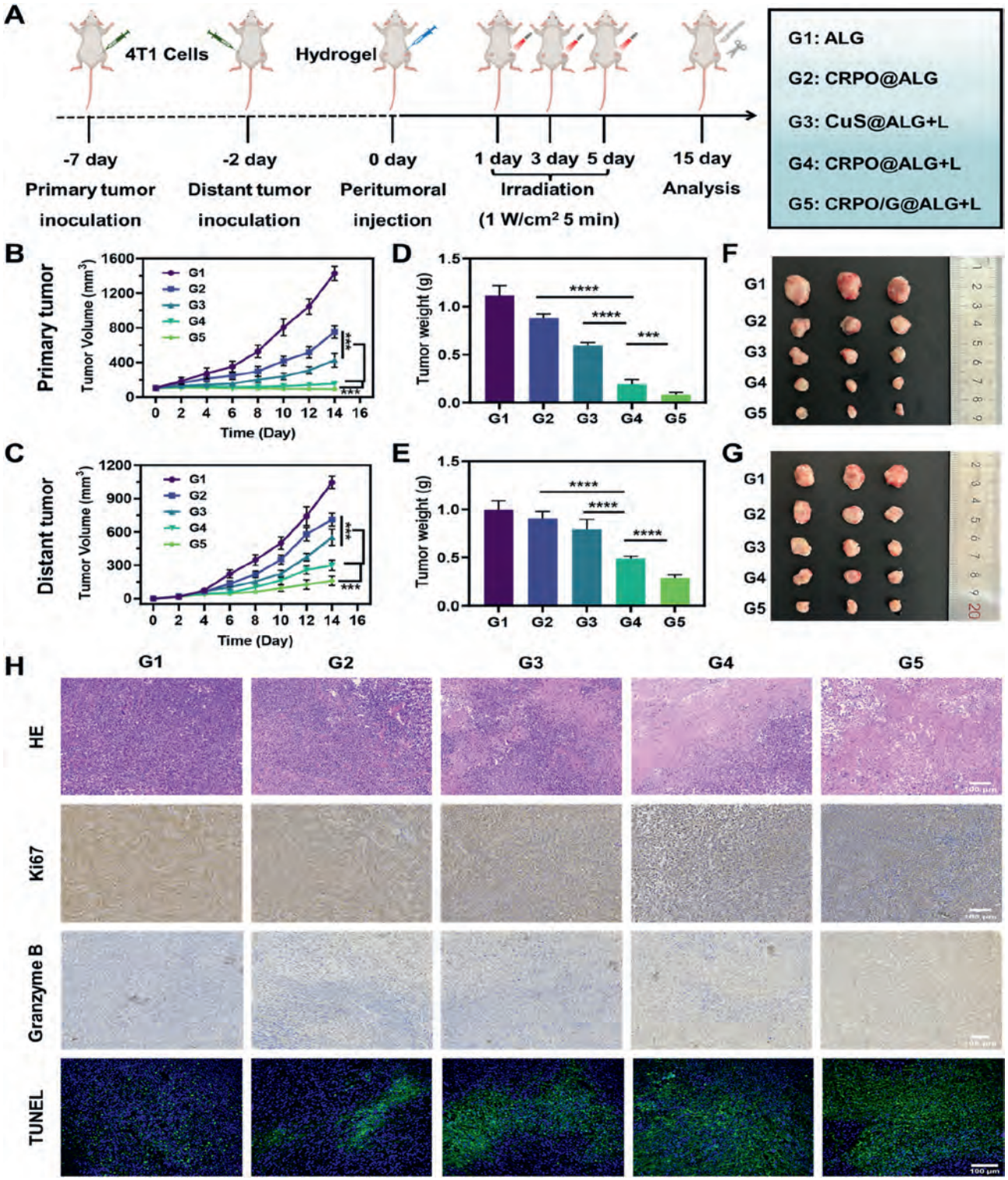

Figure 5 *In vivo* antitumor therapeutic efficacy assessment. (A) Schematic illustration of the bilateral 4T1 tumor-bearing mice model establishment and treatment schedule. (B–G) Tumor growth curves, tumor weights, and digital photos of primary and distant tumors after different treatments. (H) Immunohistochemical and immunofluorescence detection of H&E, Ki67, Granzyme B, and TUNEL staining in primary tumor sections after different treatments. Scale bar: 100 μm. The data are presented as mean ± SD ($n = 3$), and statistical significance was calculated by one-way analysis of variance (ANOVA), ***$P < 0.001$, and ****$P < 0.0001$.

(Fig. 5H). Compared to other groups, the CRPO/G@ALG with irradiation group exhibited the most severe tumor tissue damage, the most significant inhibition of tumor cell proliferation, the highest level of cytotoxic immune response, and the most extensive apoptosis. A similar trend was observed in distant tumors, corroborating its superior therapeutic efficacy (Supporting Information Fig. S8). Following this, biosafety evaluations of CRPO/G@ALG were conducted to estimate systemic toxicity and potential side effects. Throughout the treatment period, the body weight of mice in the CRPO/G@ALG with irradiation group remained stable, indicating no acute systemic toxicity (Supporting Information Fig. S9). Histological analysis of major organs (heart, liver, spleen, lungs, and kidneys) revealed no observable pathological abnormalities compared to the control group (Supporting Information Fig. S10A). Additionally, blood routine parameters and serum biochemical indices, such as hemoglobin, red blood cells, alanine aminotransferase, etc., all fell within the normal range (Fig. S10B and S10C). These findings demonstrate that CRPO/G@ALG exhibits excellent biocompatibility and minimal systemic toxicity, making it a safe and effective candidate for therapeutic applications.

3.6. In vivo antitumor immunity activation assessment

Dendritic cell-orchestrated antigen presentation represents a pivotal link between innate and adaptive immune responses[55,56]. Fig. 6A outlines this process, starting from the release of tumor antigens at the tumor site, progressing to antigen capture in the TMEs, and culminating in antigen cross-presentation within tumor-draining lymph nodes (TDLNs). The chemokine ligand 21 and chemokine receptor 7 (CCL21−CCR7) axis directs the migration of antigen-loaded DCs from the TMEs to TDLNs, where they prime naïve T cells and initiate systemic immune responses[57-60]. This dynamic cascade establishes a critical functional bridge between local antigen processing and systemic immune activation, and any disruption or inefficiency at any stage of this process can compromise immune activation[21,61]. Building on these insights, considerable efforts have been devoted to explicating the entire cascade of events in our work. In distinction from the majority of studies that primarily focus on DC maturation in the TDLNs, we also place significant emphasis on tumor infiltration, antigen capture, and antigen trafficking by DCs.

Antigen exposure and DC recruitment at the tumor site were first investigated. Immunofluorescence images of tumor sections revealed that the CRPO/G@ALG with irradiation treatment led to pronounced CRT translocation and substantial DC accumulation compared to other groups (Fig. 6B and C). As a hallmark of immunogenic cell death, CRT exposure not only reflects the release of abundant tumor-associated antigens but also serves as an "eat-me" signal to facilitate DC recruitment and antigen uptake. These findings underscore the positive impact of the CRPO/G@ALG with irradiation treatment in creating highly immunogenic TMEs and enhancing antigen capture, laying a strong foundation for effective antigen cross-presentation.

Subsequently, tumor-infiltrating DCs were analyzed by flow cytometry to further characterize the phenotype of recruited DCs. Migratory DCs ($CD11c^+CD103^+$), renowned for their exceptional capabilities in antigen uptake, processing, and transport, play a critical role in connecting local antigen capture with systemic immune activation[58,62]. Flow cytometry analysis of tumor-infiltrating DC subsets demonstrated that the CRPO/G@ALG with irradiation group exhibited the largest proportion of migratory DCs among all groups (Fig. 6D and E). Additionally, CCR7 expression on migratory DCs, upregulated by antigen capture and other stimuli such as DAMPs or adjuvants, is essential for guiding these cells to TDLNs along the CCL21 gradient established by lymphatic endothelial cells[24,57,63]. Further investigation revealed that the highest proportion of the CCR7-expressing migratory DCs was observed in the CRPO/G@ALG with irradiation group (Fig. 6F and G). These results suggest that CRPO/G@ALG optimizes antigen cross-presentation by enhancing the recruitment and migration of migratory DCs.

TDLNs are key sites for tumor antigen cross-presentation and naïve T cell priming[61]. Single-cell suspensions from TDLNs were analyzed by flow cytometry to verify the homing and activation status of DCs in TDLNs. Representative plots and statistical data uncover that the CRPO/G@ALG with irradiation group had the highest proportion of active DCs ($CD80^+CD86^+$) among all groups (Fig. 6H and I). The upregulation of these co-stimulatory molecules indicates DC maturation, which facilitates effective antigen cross-presentation and initiation of adaptive immune responses. These findings indicate that the CRPO/G@ALG with irradiation treatment promotes the homing and maturation of DCs, thereby advancing antitumor immunity activation and boosting downstream immune responses.

3.7. In vivo antitumor immunity activity assessment

The fundamental driver of adaptive antitumor immunity is T cell-mediated responses, which constitute the dominant effector mechanism for tumor cell elimination[64-66]. To comprehensively assess the antitumor immune activity induced by different treatments, flow cytometry analysis was performed to examine the phenotypes and proportions of T cells. The spleen, a central hub for immune cells, supports T cell expansion, differentiation, and activation, providing critical insights into T cell composition and functional status within systemic circulation. Representative plots and quantitative analysis revealed that the CRPO/G@ALG with irradiation group exhibited a significantly increased frequency of cytotoxic T cells (CTLs, $CD3^+CD8^+$) and helper T cells (Ths, $CD3^+CD4^+$), alongside a markedly reduced frequency of regulatory T cells (Tregs, $CD4^+Foxp3^+$), compared to other groups (Fig. 7A−F). These alterations suggest that CRPO/G@ALG with irradiation treatment promotes the expansion of antitumor effector cells and regulates the differentiation of immunosuppressive cells concurrently, confirming the successful activation of T cell-mediated systemic antitumor immunity.

Cytokines represent critical regulators of immune activation, reflecting the delicate balance between pro-inflammatory and immunosuppressive phases[67,68]. The serum levels of representative cytokines were measured to evaluate the systemic immune status of the organism (Supporting Information Fig. S11). Compared to the control group, significantly elevated levels of IFN-γ (6-fold), TNF-α (5-fold), and IL-6 (2-fold) in the CRPO/G@ALG with irradiation group indicated enhanced antitumor immunity, whereas a substantial reduction in IL-10 (2-fold) suggested alleviation of immunosuppressive conditions. These cytokine profiles underscored intensified immune activation and the shift toward a pro-inflammatory immune phase, which was associated with enhanced cytotoxic T cell activity and suppressed regulatory T cell function. These findings emphasize the potent immunomodulatory potential of CRPO/G@ALG combined with irradiation treatment in reinforcing systemic antitumor immunity.

Tumor tissues are the battleground where immune cells interact with cancer cells, demanding effective T cell infiltration,

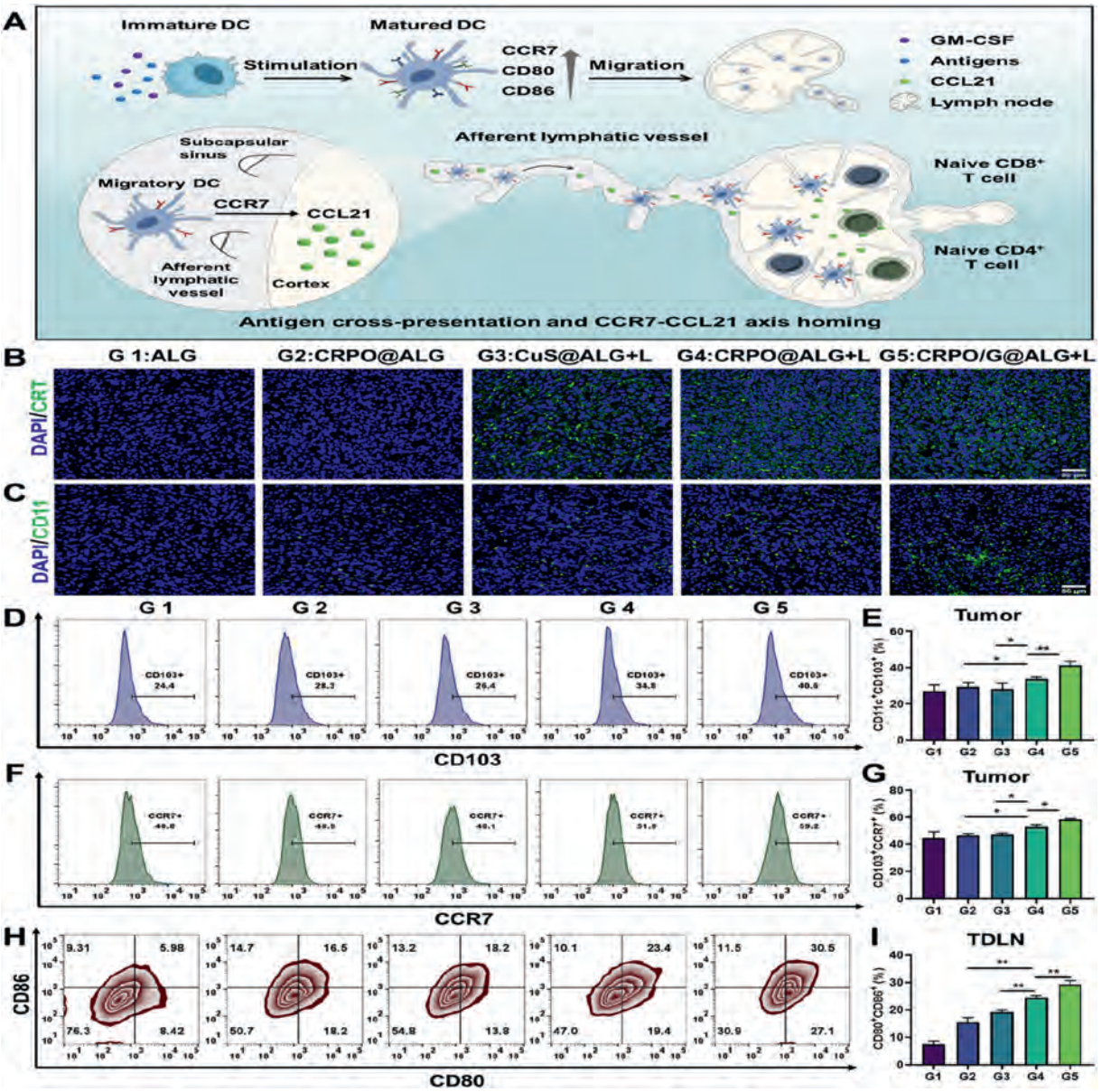

Figure 6 *In vivo* antitumor immunity activation assessment. (A) Schematic illustration of Antigen cross-presentation and CCR7−CCL21 axis homing. (B, C) Immunofluorescence staining of CRT exposure and DCs distribution in tumor sections. Scale bar: 50 μm. (D, E) Representative flow cytometry plots and quantification analysis of the proportion of migratory DCs ($CD11c^+CD103^+$) in tumors after diverse treatments. (F, G) Representative flow cytometry plots and quantification analysis of the proportion of CCR7-expressing migratory DCs ($CD11c^+CD103^+CCR7^+$) in tumors after diverse treatments. (H, I) Representative flow cytometry plots and quantification analysis of the proportion of matured DCs ($CD11c^+CD80^+CD86^+$) in tumor-draining lymph nodes after diverse treatments. The data are presented as mean ± SD ($n = 3$), and statistical significance was calculated by one-way analysis of variance (ANOVA), $^*P < 0.05$, and $^{**}P < 0.01$.

tumor-specific recognition, and killing. The immune landscape of T cells within tumors profoundly influences tumor progression and therapeutic outcomes, reflecting immune dynamics and serving as an important metric for evaluating antitumor efficacy. Mirroring the trend observed in the spleen, flow cytometry analysis of the primary tumor in the CRPO/G@ALG with irradiation group displayed the highest proportions of CTLs and Ths, along with the lowest proportion of Tregs (Fig. 7G−K). Furthermore, immunofluorescence staining of distant tumor sections corroborated these findings, demonstrating the most plentiful infiltration of CTLs and Ths, and the minimal distribution of Tregs (Supporting Information Fig. S12). The remarkable T cell-mediated tumor-specific immune response probably benefits from the abundant antigen supply, enhanced intratumoral dendritic cell accumulation, improved lymph node homing, and supplementary stimulation provided by adjuvants. Collectively, these data indicate that CRPO/G@ALG with irradiation treatment effectively reshapes the tumor immune status, boosting antitumor immune activity and favoring more efficient tumor elimination.

3.8. *In vivo lung metastasis suppression assessment*

Considering that the lung is the most prevalent site of metastasis in breast cancer, which is tightly associated with poor prognosis and

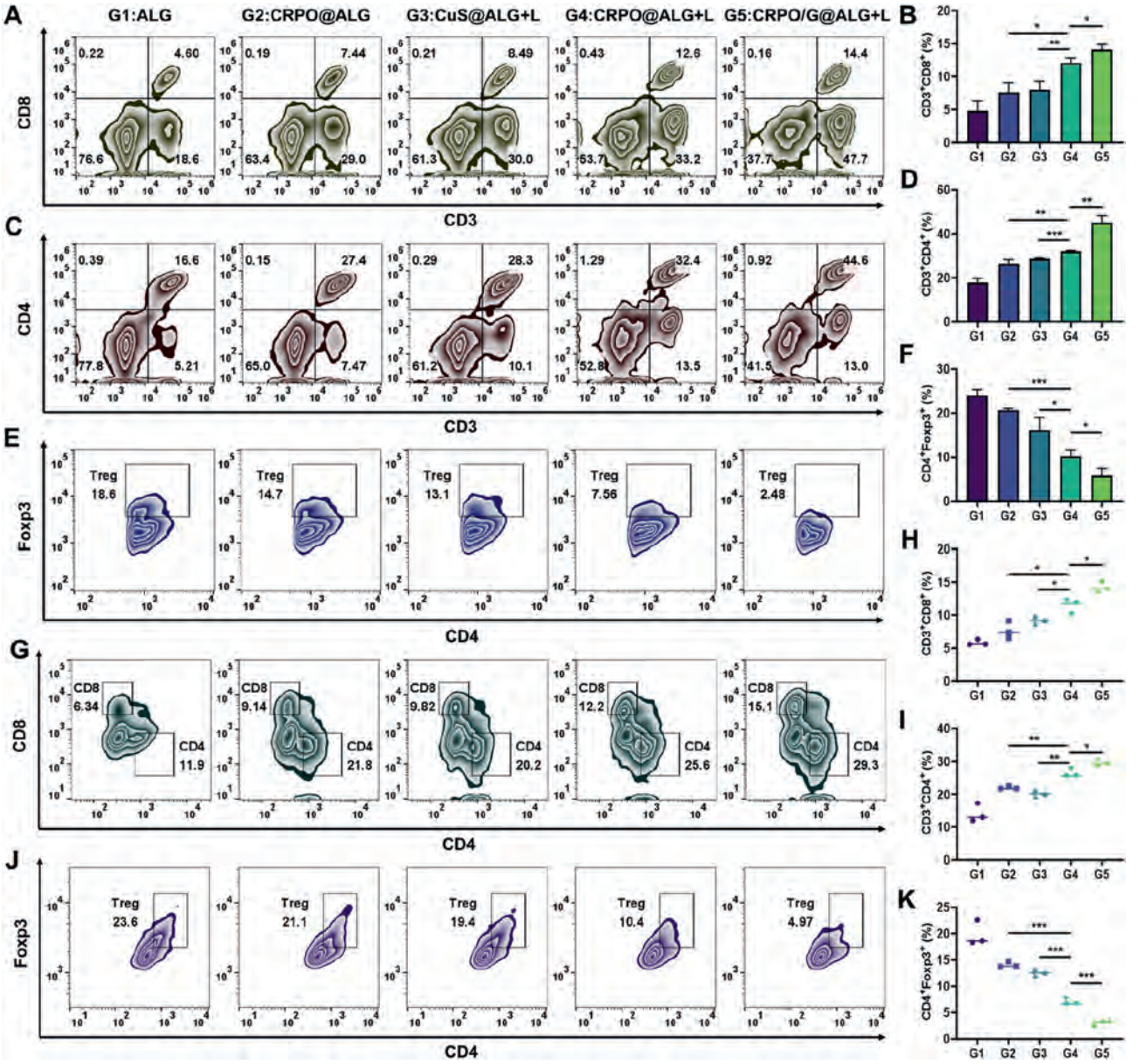

Figure 7 *In vivo* antitumor immunity activity assessment. (A, B) Representative flow cytometry plots and quantification analysis of the cytotoxic T lymphocytes ($CD3^+CD8^+$) in spleens. (C, D) Representative flow cytometry plots and quantification analysis of the helper T lymphocytes ($CD3^+CD4^+$) in spleens. (E, F) Representative flow cytometry plots and quantification analysis of the regulatory T lymphocytes ($CD4^+Foxp3^+$) in spleens. (G−I) Representative flow cytometry plots and quantification analysis of the cytotoxic T lymphocytes ($CD3^+CD8^+$) and the helper T lymphocytes ($CD3^+CD4^+$) in tumors. (J, K) Representative flow cytometry plots and quantification analysis of the regulatory T lymphocytes ($CD4^+Foxp3^+$) in tumors. The data are presented as mean ± SD ($n = 3$), and statistical significance was calculated by one-way analysis of variance (ANOVA), $^*P < 0.05$, $^{**}P < 0.01$, and $^{***}P < 0.001$.

high mortality in clinical settings[8-11]. Therefore, a lung metastasis model was established to further assess the potential for improving intervention outcomes (Fig. 8A). Numerous metastatic foci were observed in the lung tissues of the ALG control group. In comparison, mice receiving the CRPO/G@ALG combined with irradiation treatment demonstrated almost complete rejection of lung metastases (Fig. 8B). Quantitative analysis revealed a significant reduction of metastatic nodules in the CRPO/G@ALG group compared to the control, with 55.7 ± 6.2 nodules *versus* 8.3 ± 3.1 nodules, respectively (Fig. 8C). Lung tissues were subsequently subjected to pathological analysis, including HE, Ki67, and CD8 staining. In the CRPO/G@ALG with irradiation group, no detectable tumor lesions were identified, accompanied by controlled cell proliferation and increased immune cell infiltration (Fig. 8D). These findings indicated that CRPO/G@ALG with irradiation treatment effectively suppressed lung metastasis, attributed to the photoimmunological combination strategy, which induced a robust systemic antitumor immune response capable of tracking and attacking metastatic tumor cells.

The excellent therapeutic performance of CRPO/G@ALG combined with irradiation in inhibiting the progression of primary, distant, and lung metastasis tumors justifies further investigation to

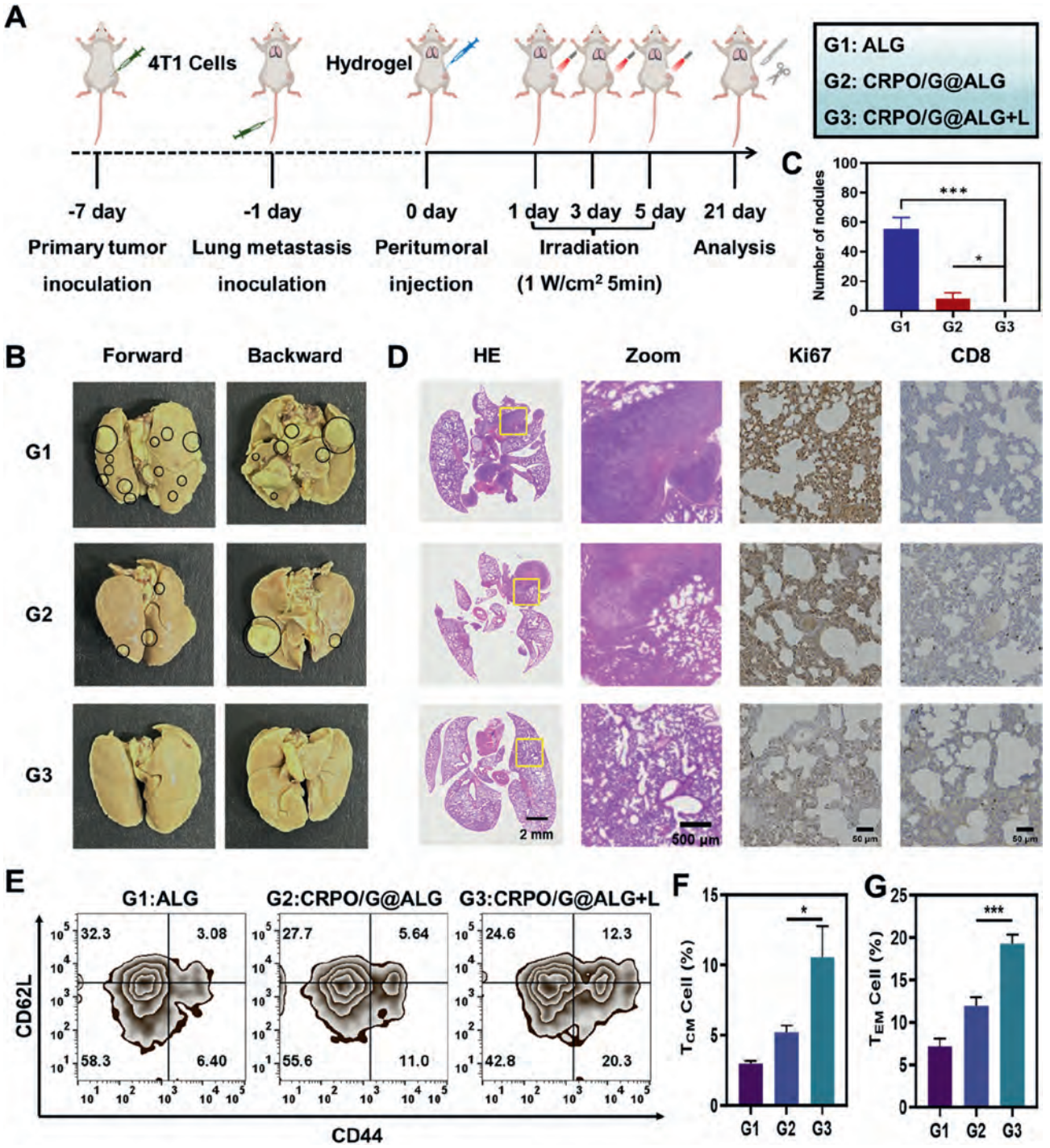

Figure 8 *In vivo* lung metastasis suppression assessment. (A) Schematic illustration of the lung metastasis 4T1 tumor-bearing mice model establishment and treatment schedule. (B) Photographs of Bouin's solution-stained lung tissues after different treatments. (C) Quantification analysis of lung metastatic nodules (D) Immunohistochemistry staining for HE, Ki67, and CD8 of the lung sections after different treatments. Scale bar: 2 mm or 50 μm. (E, G) Representative flow cytometry plots and quantification analysis of central memory T cells (T_{CM}: $CD3^+CD8^+CD62L^+CD44^+$) and effector memory T cells (T_{EM}: $CD3^+CD8^+CD62L^-CD44^+$). The data are presented as mean ± SD ($n = 3$), and statistical significance was calculated by one-way analysis of variance (ANOVA), $^*P < 0.05$, and $^{***}P < 0.001$.

explore whether it can elicit lasting antitumor immunity, which may support the prevention of tumor recurrence. To investigate the immune factors driving long-term memory responses, spleens were harvested and analyzed by flow cytometry. It is well known that antigen-specific memory T cells can be classified into central memory T (T_{CM}, $CD3^+CD8^+CD62L^+CD44^+$) cells and effector memory T (T_{EM}, $CD3^+CD8^+CD62L^-CD44^+$) cells based on their functional characteristics[64,69,70]. Among them, Tcm cells possess strong proliferative potential and provide vigorous protection through expansion, differentiation, and trafficking. On the other

hand, Tem cells can rapidly respond to secondary tumor challenges and secrete cytokines that enhance immune activity, thereby providing immediate protection. Representative flow cytometry plots and quantification analysis demonstrated that the proportion of Tcm and Tem cells was significantly increased in the CRPO/G@ALG with irradiation group compared to the CRPO/G@ALG alone group (Fig. 8E−G). These observations provide additional evidence that CRPO/G@ALG combined with irradiation treatment equips the organism with a durable immune memory effect, establishing a persistent defense against tumor relapse.

4. Conclusions

In summary, this study introduces a novel injectable photoimmunological hydrogel vaccine (CRPO/G@ALG), which significantly improves antitumor immune responses and enhances cancer therapy through dual mechanisms: immunogenic cell death (ICD) induction and dendritic cell (DC) recruitment. CRPO/G@ALG undergoes gelation in response to physiological calcium ions, enabling the localized retention and sustained release of exogenous antigens and adjuvants. These favorable drug release characteristics prolong the duration of immune stimulation and reduce the frequency of required vaccinations, offering substantial convenience for clinical applications. CRPO/G@ALG effectively triggers ICD induction under near-infrared (NIR) irradiation, establishing an *in situ* autologous antigen reservoir that expands tumor immunogenicity and enhances antigenic diversity, thus improving the quality and magnitude of adaptive immune responses. Moreover, CRPO/G@ALG successfully recruits dendritic cells (DCs) to accumulate in the tumor microenvironment, facilitating antigen capture, trafficking, and presentation, thereby providing robust support for antitumor immune activation. In the 4T1 mouse model, CRPO/G@ALG demonstrated excellent therapeutic effects. It not only significantly inhibited primary tumor growth but also effectively prevented distant tumor progression and lung metastasis formation. Taken together, CRPO/G@ALG offers an innovative and comprehensive strategy by targeting multiple stages of the cancer-immunity cycle while integrating the advantages of nanovaccines and hydrogels. This research offers a new paradigm for the development of next-generation nanocomposite-based hydrogel vaccines and lays a solid foundation for future clinical applications.

Acknowledgments

This research was supported, in whole or in part, by the National Natural Science Foundation of China (52372263, 32171395, 12132004, 32471367), the Sichuan Science and Technology Program (2024NSFSC0601, China), the Program for Innovative Fundamental Research Incubation of UESTC (Y03023206100226, China), and the Joint Innovation Fund of Health Commission of Chengdu and Chengdu University of Traditional Chinese Medicine (WXLH202403090, China) ICD (immunogenic cell death) and TEM (tumor microenvironment).

Author contributions

Hanxi Zhang: Conceptualization, Data curation, Formal analysis, Investigation, Methodology, Validation, Visualization, Writing-original draft, Writing-Review & Editing. Jiazhen Lv: Conceptualization, Data curation, Formal analysis, Investigation, Methodology, Validation, Visualization, Writing-original draft. Wanyi Zhou: Investigation, Methodology. Jiangping Lei: Investigation, Methodology. Yu Yang: Investigation, Methodology. Jianqiao Kong: Investigation, Methodology. Chunhui Wu: Methodology, Resources, Funding acquisition. Chuan Zheng: Methodology, Resources, Conceptualization. Fengming You: Methodology, Resources, Conceptualization. Yiyao Liu: Conceptualization, Supervision, Project administration, Funding acquisition, Writing-Review & Editing. Hong Yang: Conceptualization, Data curation, Supervision, Project administration, Funding acquisition, Writing-Review & Editing.

Conflicts of interest

The authors declare no conflict of interest.

Appendix A. Supplementary information

Supporting information to this article can be found online at https://doi.org/10.1016/j.apsb.2025.10.024.

References

1. Chen DS, Mellman I. Oncology meets immunology: the cancer-immunity cycle. *Immunity* 2013;**39**:1−10.
2. Hegde PS, Chen DS. Top 10 challenges in cancer immunotherapy. *Immunity* 2020;**52**:17−35.
3. Wang M, Yu F, Zhang Y. Present and future of cancer nano-immunotherapy: opportunities, obstacles and challenges. *Mol Cancer* 2025;**24**:26.
4. Mishra AK, Ali A, Dutta S, Banday S, Malonia SK. Emerging trends in immunotherapy for cancer. *Diseases* 2022;**10**:60.
5. Zhang YY, Zhang Z. The history and advances in cancer immunotherapy: understanding the characteristics of tumor-infiltrating immune cells and their therapeutic implications. *Cell Mol Immunol* 2020;**17**:807−21.
6. Saxena M, van der Burg SH, Melief CJM, Bhardwaj N. Therapeutic cancer vaccines. *Nat Rev Cancer* 2021;**21**:360−78.
7. Lin MJ, Svensson-Arvelund J, Lubitz GS, Marabelle A, Melero I, Brown BD, et al. Cancer vaccines: the next immunotherapy frontier. *Nat Cancer* 2022;**3**:911−26.
8. Leon-Ferre RA, Goetz MP. Advances in systemic therapies for triple-negative breast cancer. *BMJ* 2023;**381**:e71674.
9. Bianchini G, De Angelis CD, Licata L, Gianni L. Treatment landscape of triple-negative breast cancer-expanded options, evolving needs. *Nat Rev Clin Oncol* 2022;**19**:91−113.
10. Li Y, Zhang HJ, Merkher Y, Chen L, Liu N, Leonov S, et al. Recent advances in therapeutic strategies for triple-negative breast cancer. *J Hematol Oncol* 2022;**15**:121.
11. Agostinetto E, Losurdo A, Nader-Marta G, Santoro A, Punie K, Barroso R, et al. Progress and pitfalls in the use of immunotherapy for patients with triple-negative breast cancer. *Expet Opin Invest Drugs* 2022;**31**:567−91.
12. Liu Y, Hu YT, Xue JQ, Li JY, Yi J, Bu JW, et al. Advances in immunotherapy for triple-negative breast cancer. *Mol Cancer* 2023;**22**:145.
13. Keenan TE, Tolaney SM. Role of immunotherapy in triple-negative breast cancer. *J Natl Compr Cancer Netw* 2020;**18**:479−89.
14. Yang Z, Gao D, Zhao J, Yang GJ, Guo M, Wang Y, et al. Thermal immuno-nanomedicine in cancer. *Nat Rev Clin Oncol* 2023;**20**:116−34.
15. Duan XP, Chan C, Lin WB. Nanoparticle-mediated immunogenic cell death enables and potentiates cancer immunotherapy. *Angew Chem Int Ed* 2019;**58**:670−80.

16. Galluzzi L, Guilbaud E, Schmidt D, Kroemer G, Marincola FM. Targeting immunogenic cell stress and death for cancer therapy. *Nat Rev Drug Discov* 2024;**23**:445−60.
17. Meier P, Legrand AJ, Adam D, Silke J. Immunogenic cell death in cancer: targeting necroptosis to induce antitumour immunity. *Nat Rev Cancer* 2024;**24**:299−315.
18. Pishesha N, Harmand TJ, Ploegh HL. A guide to antigen processing and presentation. *Nat Rev Immunol* 2022;**22**:751−64.
19. Jhunjhunwala S, Hammer C, Delamarre L. Antigen presentation in cancer: insights into tumour immunogenicity and immune evasion. *Nat Rev Cancer* 2021;**21**:298−312.
20. Yang K, Halima A, Chan TA. Antigen presentation in cancer-mechanism and clinical implications for immunotherapy. *Nat Rev Clin Oncol* 2023;**20**:604−23.
21. Wculek SK, Cueto FJ, Mujal AM, Melero I, Krummel MF, Sancho D. Dendritic cells in cancer immunology and immunotherapy. *Nat Rev Immunol* 2020;**20**:7−24.
22. Mellman I, Coukos G, Dranoff G. Cancer immunotherapy comes of age. *Nature* 2011;**480**:480−9.
23. Liang F, Lindgren G, Sandgren KJ, Thompson EA, Francica JR, Seubert A, et al. Vaccine priming is restricted to draining lymph nodes and controlled by adjuvant-mediated antigen uptake. *Sci Transl Med* 2017;**9**:eaal2094.
24. Shao N, Zhou YF, Yao J, Zhang PC, Song YN, Zhang K, et al. A bidirectional single-cell migration and retrieval chip for quantitative study of dendritic cell migration. *Adv Sci* 2023;**10**:e2204544.
25. Dang BN, Duwa R, Lee S, Kwon TK, Chang JH, Jeong JH, et al. Targeting tumor-associated macrophages with mannosylated nanotherapeutics delivering TLR7/8 agonist enhances cancer immunotherapy. *J Control Release* 2024;**372**:587−608.
26. Ye J, Mills BN, Qin SS, Garrett-Larsen J, Murphy JD, Uccello TP, et al. Toll-like receptor 7/8 agonist R848 alters the immune tumor microenvironment and enhances SBRT-induced antitumor efficacy in murine models of pancreatic cancer. *J Immunother Cancer* 2022;**10**: e4784.
27. Zhang XQ, Wei ZH, Yong TY, Li SY, Bie NN, Li JY, et al. Cell microparticles loaded with tumor antigen and resiquimod reprogram tumor-associated macrophages and promote stem-like $CD8^+$ T cells to boost anti-PD-1 therapy. *Nat Commun* 2023;**14**:5653.
28. van de Laar L, Coffer PJ, Woltman AM. Regulation of dendritic cell development by GM-CSF: molecular control and implications for immune homeostasis and therapy. *Blood* 2012;**119**:3383−93.
29. Kaufman HL, Ruby CE, Hughes T, Slingluff Jr CL. Current status of granulocyte-macrophage colony-stimulating factor in the immunotherapy of melanoma. *J Immunother Cancer* 2014;**2**:11.
30. Huang HL, Li NX, Wei XD, Li QZ, Guo JH, Yang G, et al. Biomimetic "gemini nanoimmunoregulators" orchestrated for boosted photoimmunotherapy by spatiotemporally modulating PD-L1 and tumor-associated macrophages. *Acta Pharm Sin B* 2024;**14**: 1345−61.
31. Kim SH, Han RT, Han HS, Kim YM. Immune-modulative nano-gel-nano system for patient-favorable cancer therapy. *Bioact Mater* 2025;**43**:67−81.
32. Ji PP, Sun WQ, Zhang SY, Xing YQ, Wang C, Wei MY, et al. Modular hydrogel vaccine for programmable and coordinate elicitation of cancer immunotherapy. *Adv Sci* 2023;**10**:e2301789.
33. Duong HTT, Thambi T, Yin Y, Kim SH, Nguyen TL, Phan VHG, et al. Degradation-regulated architecture of injectable smart hydrogels enhances humoral immune response and potentiates antitumor activity in human lung carcinoma. *Biomaterials* 2020;**230**:119599.
34. Askari E, Shokrollahi Barough M, Rahmanian M, Mojtabavi N, Sarrami Forooshani R, Seyfoori A, et al. Cancer immunotherapy using bioengineered micro/nano-structured hydrogels. *Adv Healthc Mater* 2023;**12**:e2301174.
35. Chen FM, Wang YJ, Gao J, Saeed M, Li TL, Wang WQ, et al. Nanobiomaterial-based vaccination immunotherapy of cancer. *Biomaterials* 2021;**270**:120709.
36. Qin L, Zhang HL, Zhou Y, Umeshappa CS, Gao HL. Nanovaccine-based strategies to overcome challenges in the whole vaccination cascade for tumor immunotherapy. *Small* 2021;**17**:e2006000.
37. Mikhail AS, Morhard R, Mauda-Havakuk M, Kassin M, Arrichiello A, Wood BJ. Hydrogel drug delivery systems for minimally invasive local immunotherapy of cancer. *Adv Drug Deliv Rev* 2023;**202**: 115083.
38. Lei L, Huang D, Gao H, He B, Cao J, Peppas NA. Hydrogel-guided strategies to stimulate an effective immune response for vaccine-based cancer immunotherapy. *Sci Adv* 2022;**8**:eadc8738.
39. Peng YX, Liang S, Meng QF, Liu D, Ma KS, Zhou ML, et al. Engineered bio-based hydrogels for cancer immunotherapy. *Adv Mater* 2024;**36**:e2313188.
40. Wang J, Zhang HX, Lv JZ, Zheng Y, Li MY, Yang G, et al. A tumor-specific ros self-supply enhanced cascade-responsive prodrug activation nanosystem for amplified chemotherapy against multidrug-resistant tumors. *Acta Biomater* 2023;**164**:522−37.
41. Liang YT, Zhu HX, Wang L, He H, Wang SF. Biocompatible smart cellulose nanofibres for sustained drug release *via* pH and temperature dual-responsive mechanism. *Carbohydr Polym* 2020;**249**:116876.
42. Dong Y, Liao HZ, Yu J, Fu H, Zhao D, Gong K, et al. Incorporation of drug efflux inhibitor and chemotherapeutic agent into an inorganic/organic platform for the effective treatment of multidrug resistant breast cancer. *J Nanobiotechnol* 2019;**17**:125.
43. Shao J, Liang RP, Ding DB, Zheng XM, Zhu XD, Hu SX, et al. A smart multifunctional nanoparticle for enhanced near-infrared image-guided photothermal therapy against gastric cancer. *Int J Nanomed* 2021;**16**:2897−915.
44. Wang WX, Wang PY, Tang XT, Elzatahry AA, Wang SW, Al-Dahyan D, et al. Facile synthesis of uniform virus-like mesoporous silica nanoparticles for enhanced cellular internalization. *ACS Cent Sci* 2017;**3**:839−46.
45. Zhitomirsky B, Assaraf YG. Lysosomes as mediators of drug resistance in cancer. *Drug Resist Updates* 2016;**24**:23−33.
46. Luzio JP, Pryor PR, Bright NA. Lysosomes: fusion and function. *Nat Rev Mol Cell Biol* 2007;**8**:622−32.
47. Li J, Xie LS, Li B, Yin C, Wang GH, Sang W, et al. Engineering a hydrogen-sulfide-based nanomodulator to normalize hyperactive photothermal immunogenicity for combination cancer therapy. *Adv Mater* 2021;**33**:e2008481.
48. Li L, Liang XQ, He T, Li XC, Huang XZ, Wang N, et al. Multifunctional light-activatable nanocomplex conducting temperate-heat photothermal therapy to avert excessive inflammation and trigger augmented immunotherapy. *Biomaterials* 2022;**290**:121815.
49. Sweeney EE, Cano-Mejia J, Fernandes R. Photothermal therapy generates a thermal window of immunogenic cell death in neuroblastoma. *Small* 2018;**14**:e1800678.
50. Chang MY, Hou ZY, Wang M, Li CX, Lin J. Recent advances in hyperthermia therapy-based synergistic immunotherapy. *Adv Mater* 2021;**33**:e2004788.
51. Li ZL, Lai XQ, Fu SQ, Ren L, Cai H, Zhang H, et al. Immunogenic cell death activates the tumor immune microenvironment to boost the immunotherapy efficiency. *Adv Sci* 2022;**9**:e2201734.
52. Zhang ZZ, Pan Z, Li QS, Huang QQ, Shi LQ, Liu Y. Rational design of ICD-inducing nanoparticles for cancer immunotherapy. *Sci Adv* 2024;**10**:eadk0716.
53. Hayashi K, Nikolos F, Lee YC, Jain A, Tsouko E, Gao H, et al. Tipping the immunostimulatory and inhibitory damp balance to harness immunogenic cell death. *Nat Commun* 2020;**11**:6299.
54. Heras-Murillo I, Adan-Barrientos I, Galan M, Wculek SK, Sancho D. Dendritic cells as orchestrators of anticancer immunity and immunotherapy. *Nat Rev Clin Oncol* 2024;**21**:257−77.
55. Murphy TL, Murphy KM. Dendritic cells in cancer immunology. *Cell Mol Immunol* 2022;**19**:3−13.
56. Cabeza-Cabrerizo M, Cardoso A, Minutti CM, Pereira DCM, Reis ESC. Dendritic cells revisited. *Annu Rev Immunol* 2021;**39**: 131−66.

57. Ohl L, Mohaupt M, Czeloth N, Hintzen G, Kiafard Z, Zwirner J, et al. CCR7 governs skin dendritic cell migration under inflammatory and steady-state conditions. *Immunity* 2004;**21**:279−88.
58. Maisel K, Sasso MS, Potin L, Swartz MA. Exploiting lymphatic vessels for immunomodulation: rationale, opportunities, and challenges. *Adv Drug Deliv Rev* 2017;**114**:43−59.
59. Swartz MA. Immunomodulatory roles of lymphatic vessels in cancer progression. *Cancer Immunol Res* 2014;**2**:701−7.
60. Zhou CP, Ma L, Xu H, Huo YQ, Luo JC. Meningeal lymphatics regulate radiotherapy efficacy through modulating anti-tumor immunity. *Cell Res* 2022;**32**:543−54.
61. Karakousi T, Mudianto T, Lund AW. Lymphatic vessels in the age of cancer immunotherapy. *Nat Rev Cancer* 2024;**24**:363−81.
62. Zhang M, Yang W, Wang P, Deng Y, Dong YT, Liu FF, et al. CCL7 recruits cDC1 to promote antitumor immunity and facilitate checkpoint immunotherapy to non-small cell lung cancer. *Nat Commun* 2020;**11**:6119.
63. Johnson LA, Jackson DG. Inflammation-induced secretion of CCL21 in lymphatic endothelium is a key regulator of integrin-mediated dendritic cell transmigration. *Int Immunol* 2010;**22**:839−49.
64. Mellman I, Chen DS, Powles T, Turley SJ. The cancer-immunity cycle: indication, genotype, and immunotype. *Immunity* 2023;**56**:2188−205.
65. Enamorado M, Iborra S, Priego E, Cueto FJ, Quintana JA, Martinez-Cano S, et al. Enhanced anti-tumour immunity requires the interplay between resident and circulating memory $CD8^+$ T cells. *Nat Commun* 2017;**8**:16073.
66. Broz ML, Binnewies M, Boldajipour B, Nelson AE, Pollack JL, Erle DJ, et al. Dissecting the tumor myeloid compartment reveals rare activating antigen-presenting cells critical for T cell immunity. *Cancer Cell* 2014;**26**:638−52.
67. Cheong JG, Ravishankar A, Sharma S, Parkhurst CN, Grassmann SA, Wingert CK, et al. Epigenetic memory of coronavirus infection in innate immune cells and their progenitors. *Cell* 2023;**186**:3882−902.
68. Ivashkiv LB. Ifngamma: signalling, epigenetics and roles in immunity, metabolism, disease and cancer immunotherapy. *Nat Rev Immunol* 2018;**18**:545−58.
69. Blass E, Ott PA. Advances in the development of personalized neoantigen-based therapeutic cancer vaccines. *Nat Rev Clin Oncol* 2021;**18**:215−29.
70. Isser A, Livingston NK, Schneck JP. Biomaterials to enhance antigen-specific T cell expansion for cancer immunotherapy. *Biomaterials* 2021;**268**:120584.